

## 32. A WAVELET ANALYSIS OF PHYSICAL PROPERTIES MEASURED DOWNHOLE AND ON CORE FROM HOLES 1095B AND 1096C (ANTARCTIC PENINSULA)<sup>1</sup>

C. Lauer-Leredde,<sup>2</sup> L. Briquet,<sup>2</sup> and T. Williams<sup>3</sup>

### ABSTRACT

We analyzed downhole logging and core petrophysical measurements from Holes 1095B and 1096C of Ocean Drilling Program Leg 178 using wavelet transforms to assess the existence of sedimentary cycles. Both holes are located in the same drift deposit (~67°S, 78°W) on the continental rise off the Pacific side of the West Antarctic Peninsula, with Hole 1095B being more distal. At both drill sites, nearly continuous sedimentary sections >570 m thick were recovered, which together span roughly the past 9.6 Ma. To properly assess the significance of apparent cyclicity obtained from the wavelet transforms of the log and core measurements, we also analyzed the December insolation signal at 67°S and its truncated form, in which the signal is set to 0 if the true insolation value is <510 W/m<sup>2</sup>. Direct comparison can be made by displaying all the results as depth-wavenumber maps, which is done for the insolation signal by converting time to depth using the known sedimentation rates at Sites 1095 and 1096. We find that the depth-wavenumber maps can be quite complicated to interpret over intervals in which the sedimentation rates vary abruptly, such as for Site 1095, where the rates range from ~20 to 110 m/m.y. Thus, accurately estimating the dominant periods, even for the insolation signal where the Milankovitch periods are known to be present, is difficult, though not impossible. Because the sedimentation rates are not known exactly and have uncertainties, any dominant period may be offset from its true value. Even with these caveats, several of the data sets have cyclicity. In

<sup>1</sup>Lauer-Leredde, C., Briquet, L., and Williams, T., 2002. A wavelet analysis of physical properties measured downhole and on core from Holes 1095B and 1096C (Antarctic Peninsula). In Barker, P.F., Camerlenghi, A., Acton, G.D., and Ramsay, A.T.S. (Eds.), *Proc. ODP, Sci. Results*, 178, 1–43 [Online]. Available from World Wide Web: <[http://www.odp.tamu.edu/publications/178\\_SR/VOLUME/CHAPTERS/SR178\\_32.PDF](http://www.odp.tamu.edu/publications/178_SR/VOLUME/CHAPTERS/SR178_32.PDF)>. [Cited YYYY-MM-DD]

<sup>2</sup>Université de Montpellier II, Place Eugène Bataillon, ISTEEM, UMR 5573, GTS, cc 60, 34095 Montpellier Cedex 5, France.

[christine.lauer-leredde@dstu.univ-montp2.fr](mailto:christine.lauer-leredde@dstu.univ-montp2.fr)

<sup>3</sup>Borehole Research Group, Lamont-Doherty Earth Observatory, Palisades NY 10964, USA.

Initial receipt: 24 August 2000

Acceptance: 19 December 2001

Web publication: 1 May 2002

Ms 178SR-205

some cases (e.g., the uranium natural gamma logs for Hole 1096C), the dominant wavenumbers appear to correspond closely to the 100-, 41-, and 23-k.y. Milankovitch periods. Generally, other periods dominate over certain depth intervals, of which periods of 30–35, 50–55, and 74–78 k.y. appear to be more common. In other data sets, the dominant wavenumbers and periods vary with depth, which could indicate significant transitions in cyclicity, provided that the sedimentation rates are accurate. Two of these transitions occur at ~2.5 and 3.5–3.8 Ma, ages that appear to be contemporaneous with paleoclimate transitions determined by prior studies.

## INTRODUCTION

The principal objectives of Ocean Drilling Program (ODP) Leg 178 were to examine Cenozoic depositional processes and climate change along the glacially influenced continental margin of the Antarctic Peninsula. The Antarctic Ice Sheet, involved in deep- and bottom-water formation and past eustatic sea level changes, is a major component of the global climate system. Unfortunately, the history of the Antarctic Ice Sheet is only partially known, primarily because it has been inferred from low-latitude proxy data (e.g., oxygen isotopic measurements).

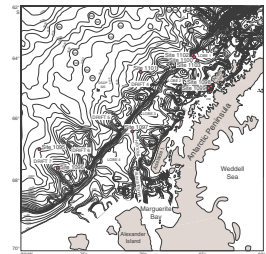
During Leg 178, nine sites were drilled on the Pacific continental margin of the Antarctic Peninsula in three depositional environments (Shipboard Scientific Party, 1999a). These included a transect of the outer continental shelf prograded wedge (Sites 1097, 1100, 1102, and 1103) and sites on two hemipelagic drifts on the continental rise (Sites 1095, 1096, and 1101), as well as two sites (1098 and 1099) on an inner-shelf basin, Palmer Deep (Fig. F1). Here, we focus on two of the continental rise sites (1095 and 1096), drilled and logged to examine the fine-grained sediments of a sediment drift. These sediments, transported from the shelf to the drift by turbidity and bottom currents (e.g., McGinnis and Hayes, 1995; Rebesco et al., 1996, 1997, 1998), contain a complete and high-resolution glacial record from 0 to 10 Ma.

The major objective of this study is to answer the question of whether deposition within the drift was cyclic. We aimed to derive the main cycles from petrophysical measurements made downhole and on cores. These data reflect physical and chemical variability in the sedimentary section, which are likely related to climatic variations. Our study is based on the powerful method of Morlet wavelet transform (Barthes and Mattei, 1997), which allows the time-frequency or depth-wavelength transform of log and core data to deduce reliable paleoclimatic information.

## GEOLOGIC SETTING AT SITES 1095 AND 1096

Sites 1095 and 1096 are located on a hemipelagic sediment drift on the continental rise off the northwestern Pacific margin of the Antarctic Peninsula (Fig. F1). These two sites are complementary and together cover the last 10 m.y., which spans most of Antarctic Peninsula glacial history. The expanded upper part of the sedimentary section within the drift was obtained at Site 1096, close to the crest of the drift, and the lower part of the drift section was obtained at Site 1095, where the overlying sediments are thinner than at the drift crest.

F1. Bathymetric chart, p. 18.



### Site 1095

The 570-m-thick sedimentary section extends from the Holocene to the early late Miocene. This section is composed of alternations of predominantly fine-grained terrigenous and hemipelagic deposits and is divided into three depositional units (Shipboard Scientific Party, 1999b). The uppermost 50 m consists of laminated and massive, often extensively bioturbated, diatom-bearing silty clays. Lithostratigraphic Unit II extends from 50 to 435 meters below seafloor (mbsf) and consists mainly of green laminated silts and muds of Pliocene and late Miocene age. Mean sedimentation rates vary from ~2 to 11 cm/k.y., based on the magnetostratigraphic record (Shipboard Scientific Party, 1999b). The sediment cores exhibit meter-scale cycles between structureless, intensely bioturbated mud sections and sections of abundant thin silt laminae (distal turbidites). These alternations are interpreted as glacial cycles that controlled sediment supply (Shipboard Scientific Party, 1999b). Longer-period variations in construction of the continental shelf may be reflected in coarsening- and fining-upward trends. Sediments below 435 mbsf consist of nonbioturbated parallel-laminated siltstone-claystones. This facies (thin-bedded turbidites) does not show the second-order cyclic pattern observed in overlying sediments, which may be significant for understanding glacial history. Sedimentation rates are higher, reaching 12 cm/k.y.

### Site 1096

The 607-m-thick sedimentary section extends in age from the Holocene to the early Pliocene (~4.7 Ma). Sediments are predominantly fine grained and terrigenous and are divided into three depositional units (Shipboard Scientific Party, 1999c). Unit I (0–33 mbsf) consists of laminated and massive, often intensely bioturbated, diatom-bearing silty clays of Pleistocene age. Unit II is an upper Pliocene to Pleistocene partly turbiditic succession some 140 m thick (33–173 mbsf) with a generally low calcareous biogenic component. Sedimentation rates average 9 cm/k.y. Sediments below 173 mbsf (Unit III), Pliocene in age, exhibit alternations of very thinly laminated and generally nonbioturbated clays and intensely bioturbated homogenous silty clays with a higher biogenic component. Overall, Unit III has a sedimentation rate of 18 cm/k.y.

In Units II and III, the alternation of laminated sediments (interpreted as turbidite facies) and bioturbated hemipelagic facies records cyclic fluctuations in sediment supply and transport processes. Some of these fluctuations may be related to glacial–interglacial cycles along the Antarctic Peninsula margin, but longer-period cycles appear to exist.

## PHYSICAL PROPERTIES DATA

### Downhole Measurements

The purposes of downhole physical properties measurements during Leg 178 were to provide near-continuous and submeter-scale records for hole-to-hole correlation and estimates of sediment properties, which can be used to reconstruct glacial and interglacial/proglacial depositional processes.

At the completion of coring operations at Sites 1095 and 1096, we logged the deepest holes (Holes 1095B and 1096C) using standard wire-line techniques. The depths of investigation are sensor dependent, and data are recorded at intervals of 15.24 cm (0.5 ft). We completed two downhole logging runs in Hole 1095B (Shipboard Scientific Party, 1999a): a triple combination (TC) (lithodensity, porosity, resistivity, and natural gamma ray) log and a geological high-sensitivity magnetic tool (GHMT) log. Logging operations were hindered by the intermittent approach of icebergs and heavy ship heave, which was large enough to cause damage to some of the logging tools. Thus, we only ran the integrated porosity-lithology tool (IPLT) (natural gamma ray, porosity, and density) and the GHMT (natural gamma ray, magnetic susceptibility, and total magnetic field) strings in Hole 1096C (Shipboard Scientific Party, 1999b). As we encountered a blockage at 343 mbsf during the first IPLT run, we logged this hole in two sections.

Borehole caliper measurements showed that Hole 1095B was typically 40–45 cm (15.7–17.7 in) in diameter (Fig. F2), with some zones of wider washout beyond the maximum caliper extent of 47 cm (18.5 in). The washed-out zones resulted in poor contact with the borehole wall and hence poor quality for the density and porosity logs. The deeper penetrating logs, such as medium resistivity (IMPH) and magnetic susceptibility (MAGS), are much less affected by changing borehole diameter (Fig. F2). We can divide the sequence into two units on the basis of changes in the character of the downhole logs (Fig. F2). Within Unit 1 (100 [base of pipe] to 510 mbsf), we note a downhole increase in the base level of susceptibility variations, with a boundary marked by a (downhole) step decrease at 325 mbsf. The lower part of this unit contains a pattern that repeats about three times (Fig. F2). Each repetition is ~40 m thick and shows a steady uphole increase in resistivity and spectral gamma ray (HSGR), topped by a sharp decrease; magnetic susceptibility behaves in the opposite way. The transition from Unit I to Unit II (510–570 mbsf) is marked by a step increase downhole in resistivity, spectral gamma ray, and magnetic susceptibility, with a slight increase in variability for resistivity and magnetic susceptibility logs.

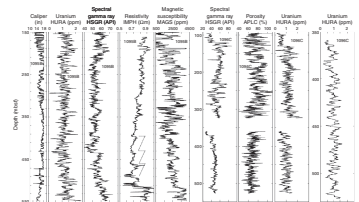
Hole 1096C was also very wide. Thus, the density and porosity logs should be regarded with caution, although neither displays the spikes that are characteristic of bad contact of the tool with the borehole wall (Fig. F2). Because of the interrupted logged depth intervals, we can not divide the formation into units on the basis of the logs alone. The logs are rich in variability, which can be related to the alternations seen in the cores.

The downhole logs were interactively depth-shifted with reference to the natural gamma ray by the Borehole Research Group (BRG) at Lamont-Doherty Earth Observatory (LDEO), and natural gamma ray data were corrected for borehole size and type of drilling fluid. As large and/or irregular borehole adversely effects recordings that require eccentricization and a good contact with the borehole wall, the porosity and density data measured in Hole 1095B were not processed with wavelets.

### Core Measurements

The physical properties measurements were made with a multisensor track (MST), which combines four sensors on an automated track for measuring whole-core magnetic susceptibility, bulk density (by gamma ray attenuation), *P*-wave velocity, and natural gamma ray emission. Whole-core magnetic susceptibility, bulk density, and *P*-wave velocity

**F2.** Measurements, Holes 1095B and 1096C, p. 19.



were measured every 2 cm, whereas natural gamma was measured every 15 cm. Color spectral reflectance (lightness parameter  $L^*$ ) was then measured on the split core at 5-cm intervals (Fig. F3) using a spectrophotometer (Shipboard Scientific Party, 1999a).

Before applying the wavelet analysis, the raw data were smoothed using a five-point running average. There are very large gaps in core measurements, due to the incomplete recovery of cores. For Hole 1096C, these gaps occur between 123 and 255 mbsf (Fig. F3). To avoid spurious features that could result from the interpolation over these gaps, we use only the data from below 255 mbsf. We then split the data into several files to eliminate the zones without core recovery over more than 4 m (e.g., Hole 1096C lightness parameter  $L^*$  from 378 to 386 mbsf) (Fig. F3). The interpolation over these zones would have given spurious results with the wavelets analysis. The same process was performed for the data from Hole 1095B. Each interval was interpolated every 2, 5, or 15 cm to be later analyzed separately.

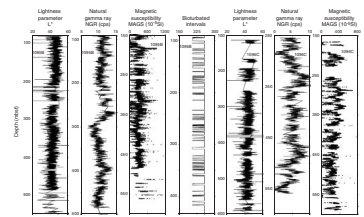
We also constructed a signal representing the bioturbated intervals and their localization in depth (Fig. F3). For that, we first digitized the master lithostratigraphic column showing dominant lithology of Hole 1095B (from Shipboard Scientific Party, 1999b) and then extracted the numerical components as a function of depth. The depth resolution of the resulting bioturbation log is controlled both by the space between the finest and closest bioturbated levels and by the number of pixels in the image. The estimated resolution here is ~30 cm. Even if this resolution is much lower than the actual core descriptions, we thought it would be interesting to analyze this signal because these bioturbated intervals might be representative of the sea temperature, currents, sediment supply, or some other property directly related to climatic variations.

The natural gamma ray (NGR) count in Hole 1095B shows an overall decrease with depth. Between 270 and 300 mbsf, it decreases sharply from ~13.5 to 7 counts per second (cps), which is not matched in the downhole log measurements (Figs. F2, F3). The gamma ray count in Hole 1096C shows an increase with depth in the first 60 mbsf, followed by a broad decrease with depth to the base of hole, possibly with a weak 50-m cyclicity (Fig. F3). There is also an inverse correlation between the NGR data and the biogenic component of the sediments (Shipboard Scientific Party, 1999c).

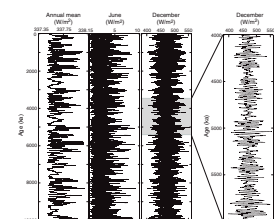
### Insolation Signal

We can compute theoretical insolation received by the Earth from its orbital parameters and its obliquity and precession (e.g., Bretagnon, 1974; Berger, 1976, 1978; Berger et al., 1989; Laskar, 1988, 1990, 1993, 1999). The insolation curve is of great interest, for it represents the major input in terms of paleoclimatic changes such as alternations of glacial–interglacial periods and of global ice volume. We computed the insolation at 67°S (the latitude of Sites 1095 and 1096) to identify the main cycles present in this signal and compare them with the cycles registered in the sediments of Holes 1095B and 1096C. We obtained the insolation for each month of the year using the program La93 developed by J. Laskar (1993, 1999). The insolation, sampled every 1000 yr, was computed over the last 10 m.y., the time interval of our study (Fig. F4). We then converted the insolation from age to depth (using the geomagnetic reversals age model presented in the next paragraph) to be homogeneous with downhole and core data.

**F3.** Bioturbated interval signals, Hole 1095B, p. 20.



**F4.** Insolation signals computed at 67°S, p. 21.



## Age Models

When we perform spectral analyses for a signal as a function of depth, we obtain wavenumbers in cycles per meter. The next step is to transform these wavenumbers into periods (kiloyears per cycle) using the sedimentation rates. As the variations in sedimentation rate for both sites are significant, the use of an average sedimentation rate over the entire section was not accurate enough. We therefore used the sedimentation rates inferred from geomagnetic reversal identifications on split cores or the GHMT log (Shipboard Scientific Party, 1999b, 1999c), as discussed in “Time-Frequency Analysis Results and Discussion,” p. 7. The overall trend for Site 1095 is an uphole decrease in sedimentation rate from ~11 cm/k.y. near the base of the hole to ~2.5 cm/k.y. at the top (Fig. F5A). Site 1096 sedimentation rates show two main intervals: from the bottom of the hole to a depth of 216 mbsf, the sedimentation rate averages ~18 cm/k.y., and above this interval, ~9 cm/k.y. (Fig. F5B). For Site 1095 we also used the sedimentation rates inferred from radiolarian and diatom data (Fig. F5A) to compare the results and estimate the discrepancies induced by the different age models.

## WAVELET TRANSFORM METHOD

The use of wavelet transforms in geophysics is relatively recent (e.g., Foufoula-Georgiou and Kumar, 1995; Kumar and Foufoula-Georgiou, 1997). The wavelet transform represents an alternative to the classical spectral analyses, such as the fast Fourier transform (FFT) or Gabor transform (Carmona et al., 1998), for time-frequency analysis; it allows not only frequency but also time localization. Wavelet transform then enables us to analyze nonlinear and nonstationary signals that contain multiscale features such as downhole logging measurements or core petrophysical measurements.

The algorithm we applied to our data sets is the one developed by Barthes and Mattei (1997), based on the theory initiated by Morlet et al. (1982a, 1982b) and later formalized by Grossman and Morlet (1984), Goupillaud et al. (1984), and Meyer (1992). The coefficient,  $W$ , of the wavelet transform can be defined as the convolution product of a signal,  $s(t)$ , function of time,  $t$ , by functions obtained by dilatation (or contraction) and temporal translation of a function,  $\Psi(t)$ , called the “mother wavelet:”

$$W(b,f) = \sqrt{f} \int_{-\infty}^{+\infty} s(t) \Psi[f(t-b)] dt, \quad (1)$$

where,

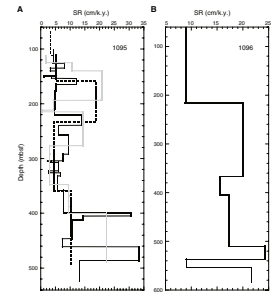
- $f$  = frequency,
- $b$  = a time or depth localization real parameter, and
- $\Psi$  = the analyzing wavelet function.

The factor,  $\sqrt{f}$ , allows for normalization.

One drawback of this definition is that the values of the time-frequency resolution of the analyzing wavelet depend on the frequency:

$$\Delta t = f^{-1} \sqrt{\frac{\ln 2}{a}}, \Delta f = f \sqrt{\frac{a \ln 2}{\pi}}, \quad (2)$$

F5. Sedimentation rates vs. depth, Sites 1095 and 1096, p. 22.



where  $a$  is a parameter that allows us to tune time/frequency resolution (dilatation/contraction of the mother wavelet).

To overcome this difficulty and obtain constant resolution, whatever the frequency, both in time and frequency, Barthes and Mattei (1997) took  $a$  proportional to  $f^{-2}$ . The wavelet transform is then redefined as

$$W(b, f) = \int_{-\infty}^{+\infty} s(t) \Psi[f(t - b)] dt \quad (3)$$

The Morlet wavelet used in this work is a locally periodic wavetrain. It is obtained by taking a complex sine wave and localizing it with a Gaussian (bell-shaped) envelope:

$$\Psi(x) = e^{-ax^2} \times e^{2\pi i x} \quad (4)$$

We selected this wavelet because its form is similar to the signals in our data. For more information about the choice of a mother wavelet, see Torrence and Compo (1998).

The Morlet wavelet is a complex wavelet that can be decomposed into real and imaginary parts (Fig. F6). The results in the time-frequency domain can be presented in three ways: the real part, the modulus, or the phase of the wavelet coefficients. Because interpretation of the phase is more complex, we chose to represent on a time-frequency map the real part or the modulus of the results in the following discussion. In this case, a periodic signal appears as a crest (straight and horizontal contour lines), and amplitude modulation of this signal will modulate the amplitude of the crest (ellipsoidal contours).

## TIME-FREQUENCY ANALYSIS RESULTS AND DISCUSSION

We investigated the downhole logs and core measurements by means of the wavelet transform to identify basic features of the power spectra and to check the fluctuations of their amplitudes and wavenumbers. The wavenumber ranges are, respectively, 0–0.75 and 0–0.8 cycles/m. The wavenumbers,  $f$ , found by the wavelet analysis were transformed into periods,  $T$  (in kiloyears), using the different sedimentation rates, SR, in centimeters per kiloyear (Fig. F5):

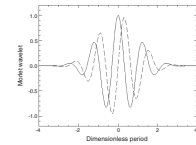
$$T = 100 \times SR^{-1} \times f^{-1} \quad (5)$$

Before dealing with the results, we have to point out the sources for periods uncertainty. Equation 5 allows us to obtain the relative errors as follows:

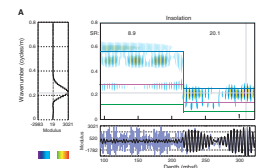
$$\Delta T/T = \Delta f/f + \Delta SR/SR \quad (6)$$

The wavelet method permits us to constrain the error in defining the wavenumbers ( $\Delta f/f$ ). As the choice of a suitable wavenumber resolution ( $\Delta f$ ) is an important issue for the wavelet method, we ran several tests in order to assess the influence of the wavenumber resolution ( $\Delta f$ ) value. We modified this parameter from 0.0005 to 0.1 cycles/m. As mentioned in “Wavelet Transform Method,” p. 6, the smaller this parameter, the better the resolution of the wavenumbers, but the lower the depth resolution. Figure F7 illustrates this artifact by showing three maps ob-

F6. Real and imaginary parts of the Morlet wavelet, p. 23.



F7. Insolation converted to depth scale and magnetic susceptibility, p. 24.

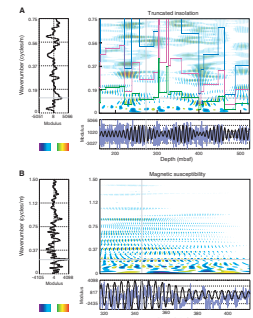


tained with  $\Delta f = 0.01$  cycles/m. If we compare them with the ones obtained for the same signals, but with  $\Delta f = 0.002$  cycles/m (Figs. F8B, F9A, F9B), we see that the low wavenumber resolution ( $\Delta f = 0.01$ ) does not resolve wavenumbers that are close to each other. For example, we only note one large feature centered at 0.480 cycles/m on Figure F7A and F7B for the insolation signals, whereas the maps of the wavelet analysis applied to the same signals with  $\Delta f = 0.002$  show two precise wavenumbers at 0.474 and 0.500 cycles/m (Fig. F9A, F9B). These examples also allow us to verify that the uncertainty in defining the wavenumbers is about four times the value of the parameter  $\Delta f$ .

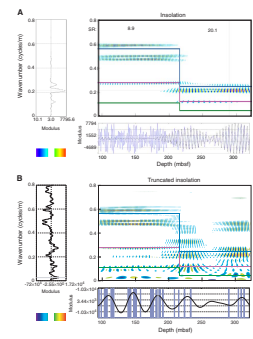
Whereas the depth limits are clear at low wavenumber resolution (Fig. F7), certain dominant wavenumbers appear to extend across intervals in which the sedimentation rate varies at high wavenumber resolution. This is the case for the insolation signals (Figs. F9A, F9B vs. F7A, F7B) or for the core magnetic susceptibility from Hole 1095B (Figs. F8B vs. F7C). We finally chose 0.002 cycles/m for  $\Delta f$ , the best compromise between the two resolutions. This choice indeed allows us to work at a high wavenumber resolution, with an uncertainty of  $\pm 0.008$  cycles/m, which means a mean error of  $\sim 10\%$ , as well as to distinguish the main limits in depth due to the attenuation of the wavenumber modulus amplitude. However, some dominant wavenumbers may be somewhat smeared when represented in the depth-wavenumber maps (with  $\Delta f = 0.002$ ) and sometimes appear to remain constant across the plot. To facilitate the analysis of these maps, we synthesize the statistically significant wavenumbers (e.g., Torrence and Compo, 1998) and their intervals of appearance more precisely in Tables T1, T2, T3, and T4, for the following results.

The limiting factor is here the uncertainty induced by the differences between the different age models ( $\Delta SR/SR$ ). As mentioned above, we use the geomagnetic reversal age model (Fig. F5) to convert the insolation signal from time to depth and to compute the periods. Confidence in the interpretation of such wavenumber/depth maps is dependent on the accuracy of the age model. The occurrence of the fundamental Milankovitch periods is greatly dependent on the sedimentation rate, as illustrated in Figure F10A; the wavenumbers corresponding to the 20-k.y. period are drastically different, depending on whether we use the geomagnetic reversal, diatom, or radiolarian age models. To give a better idea of these uncertainties, we present in Table T5 some periods computed from the thorium/potassium ratio results (Fig. F10A), using the different age models (Fig. F5). We choose the depth interval 165–195 mbsf, which corresponds to constant sedimentation rates for each model and to one of the main disagreements between the three age models. For this interval, characterized by low wavenumbers (Table T5; Fig. F10A), the sedimentation rates inferred from radiolarian and diatom data are nearly four times higher than the one induced from geomagnetic reversals (Fig. F5). This ratio recurs for the computed periods, leading to very different interpretations. When we use the geomagnetic reversal age model, the periods are long, comparable to the Milankovitch eccentricity period (Table T5). On the contrary, the radiolarian and diatom age models lead to shorter periods, close to the Milankovitch precession and obliquity periods (Table T5). This case, though extreme, shows that this point has to be kept in mind when considering the next results, as it might introduce relative uncertainties in the periods, especially over the intervals where the discrepancies between the different models is important. The uncertainty induced by the age

F8. Insolation, magnetic susceptibility, and bioturbated intervals, Hole 1095B, p. 26.



F9. December insolation and reflectance, Hole 1096C, p. 28.



T1. Wavelet analysis of insolation, natural gamma ray, and thorium/potassium logs, Hole 1095B, p. 38.

T2. Wavelet analysis of magnetic measurements, Hole 1095B, p. 39.

T3. Wavelet analysis of insolation, porosity, gamma ray, and uranium logs, Hole 1096C upper section, p. 40.

T4. Wavelet analysis of insolation signal, porosity, and uranium logs, Hole 1096C lower section, p. 41.

models for Hole 1095B varies from a few percent, when the age models are in agreement, to ~75%.

### Insolation Signal

Before in-depth analysis, we applied the wavelet analyses to the signal previously computed as a function of time (Fig. F4). This preliminary treatment shows how Milankovitch periods are present in the insolation signal at 67°S and how the transition between time/frequency and depth/wavenumber affect the wavelet analysis.

As expected, the annual mean insolation is very sensitive to the 40-k.y. period, the Milankovitch cyclicity related to changes of the Earth's obliquity. This parameter, which affects seasonality and insolation gradient, has greatest effect in high latitudes (e.g., Imbrie and Imbrie, 1979).

This obliquity period is still present on the spectral map of June and December insolation signals, which correspond, respectively, to the minimum and maximum of insolation received by the Earth (Fig. F11A, F11B). This frequency (0.025 cycles/k.y.) presents alternations of its intensity (e.g., stronger between 1.98 and 2.88 Ma, weaker between 2.88 and 3.28 Ma, and stronger between 3.28 and 4.08 Ma). The two maps also reveal very strong frequencies at 0.043 and 0.052 cycles/k.y., the Milankovitch 19- and 23-k.y. cycles, related to precession that affects the radiation intensity for each season. Contrary to the spectral map for December insolation, we observe frequencies different from those of Milankovitch, though much weaker, on the spectral map for June insolation (Fig. F11A): 0.01 cycles/k.y. (100 k.y.; eccentricity that affects total insolation), 0.02 cycles/k.y. (~50/52 k.y.), 0.033 cycles/k.y. (~30 k.y.), 0.067 cycles/k.y. (~15 k.y.), 0.087 cycles/k.y. (~11.5 k.y.), and 0.095 cycles/k.y. (~10.5 k.y.).

To enhance the contribution of other wavenumbers to the spectrum, we truncated the December insolation values by setting those values <510 W/m<sup>2</sup> to 0. We speculate that it is the high insolation values that control the extent of the ice sheet and, hence, the supply of glacial sediment to the drifts. The spectral map contains the previous Milankovitch periods but also contains others with significant amplitude (Fig. F11C): 200/330 k.y., 100 k.y.; 50–55 k.y., 30 k.y., 15/16 k.y., and 12/13 k.y. These periods effectively present in the insolation signal (Fig. F11A) (e.g., Laskar, 1993) but with amplitudes much lower than the obliquity and precession periods are better revealed on the truncated December insolation map.

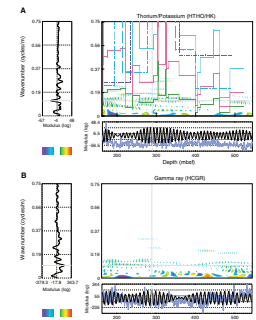
### Hole 1095B

The wavelet analysis was performed for four types of signals: the logs (recorded each 15.24 cm), the core physical properties measurements (recorded each 2, 5, or 15 cm), the bioturbated beds, and the December insolation signals (interpolated each 5 cm). To be able to compare the results, the insolation signals were converted to a depth scale and analyzed on the same depth interval as the logs (165–545 mbsf) (i.e., ~3–9 Ma).

Some representative wavenumber maps are presented in Figures F8 and F10, and all the results are synthesized in Figure F12.

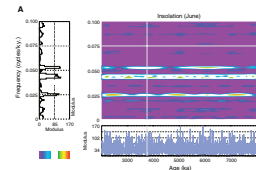
The alternation of glacial–interglacial cycles induces discontinuities in the sedimentary processes. This alternation being related to changes in insolation maxima, we assume that the wavelet analysis of the trun-

**F10.** Thorium/potassium and natural gamma ray logs, Hole 1095B p. 30.

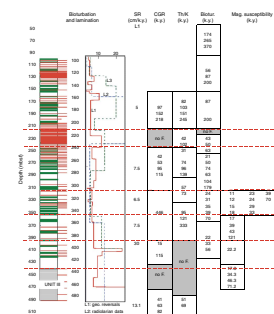


**F5.** Wavelet analysis of thorium/potassium logs, Hole 1095B, p. 42.

**F11.** June and December insolation signals, p. 31.



**F12.** Synthesis combining all results for Hole 1095B, p. 33.



cated insolation emphasizes these discontinuities. This truncated form contains the periods present in the total signal, essentially the precession of 19- and 23-k.y. periods. The analysis of this signal also reveals other periods, such as 103, 128, 133, 392, and 439 k.y. in the low wavenumber domain, and 10, 12, and 13 k.y. in the high wavenumber domain.

For this site, we concentrate on the gamma ray and thorium/potassium ratio logs (representative of the different type of clays present in the formation) (e.g., Serra, 1979, 1985; Ellis, 1987), core magnetic susceptibility measurements, and bioturbated interval results (Figs. F8, F10). The complete wavenumber content of all the signals analyzed by wavelet transform is presented in Table T1. As sedimentation rates (SRs) for this site are highly variable, the wavenumbers were transformed into periods using the average SR of the interval where they appear (Fig. F12).

We chose these signals because the comparison of the main periods, recognized in their maps (Figs. F8, F10) allows us to divide the different geological units defined from core description (Shipboard Scientific Party, 1999b) into subunits (Fig. F12). The lower and middle part of Unit II (143–436 mbsf) can be subdivided in five subunits: 140–220, 220–250, 250–320, 320–390, and 390–400 mbsf. Of course, if we look precisely at the maps (Figs. F8, F10), it is clear that the limits are gradual rather than sharp and that the overlap between the wavenumber bands is ~15 m. This is because we favored the high-frequency resolution to the detriment of the spatial resolution; there is a trade-off between the two.

The downhole logs cover the depth interval from 165 to 545 mbsf, from the Miocene (9.6 Ma) to mid-Pliocene (4.3 Ma) time period, according to geomagnetic reversal identification (Shipboard Scientific Party, 1999b). The logs acquired in Hole 1095B do not appear to allow resolution of wavenumbers above ~0.4 cycles/m (Fig. F10). This possibly results from the vertical resolution of the logs, which varies between 30 and 70 cm. The strong heave encountered during logging might also have enhanced the noise that overprints the high wavenumbers domain. In contrast, the information extracted from the core measurements, acquired at a centimeter scale, is much richer in the high-wavenumber domain. In particular, the results correlate very well between the bioturbated beds and core magnetic susceptibility signals for the subunit from 320 to 390 mbsf (Fig. F12). The 24-, 33-, 39-, and 74-k.y. periods are well evidenced, with high modulus (Figs. F8B, F8C; Table T1). The deposit in this subunit was certainly controlled by cyclic processes, some of them being close to Milankovitch precession and obliquity periods. The core magnetic susceptibility allows us to divide this subunit into two parts at the depth of 355 mbsf (Fig. F12). The first interval is mainly characterized by high wavenumbers, contrary to the second one. This shift at ~8 Ma, which corresponds to an abrupt change of low sedimentation rates toward higher ones for the three different age models (Fig. F5), might then be a major transition. The wavenumbers occurring within this particular unit are summarized for the core magnetic susceptibility analysis in Table T2 and again illustrate how different the periods derived from these wavenumbers can be, depending on the age model used. The discrepancies are particularly obvious for the upper part of this subunit, from 320 to 355 mbsf, where the SR is multiplied by ~2.5. For the lower section (355–390 mbsf), the age models are closer. Here, the signal contains the ~41-k.y. period, the Milanko-

vitch cyclicity related to changes of the Earth's obliquity, and is dominated by the ~100-k.y. period (eccentricity).

### Hole 1096C

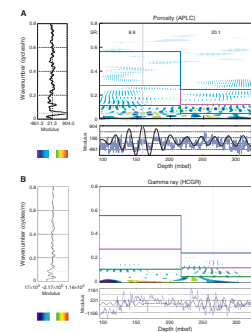
As previously mentioned, Site 1096 was drilled to sample the shallow part of the stratigraphic section within the drift. It complements Site 1095, where the youngest sediments are thinner. Hole 1096C then allows us to examine at high time resolution the cyclicity in a highly expanded Pliocene–Pleistocene section. If we look at the ages according to geomagnetic reversal identification (Shipboard Scientific Party, 1999b, 1999c), our downhole logging data for Hole 1096C end at ~4.2 Ma (525 mbsf), which corresponds to ~130 mbsf for Hole 1095B. Therefore, we are not able to compare the logs over the same time interval in the two holes.

As for Hole 1095B, the wavelet analysis was performed for the logs, the core physical properties measurements, and the December insolation signals (both truncated and not truncated). For the logs, the analysis was done using two segments of data because of the interruption of logging (Fig. F2). The upper section, from 95 to 325 mbsf, corresponds to the late Pliocene and the early Pleistocene time interval, between ~1.2 and 3.1 Ma. This section encompasses the Unit II/Unit III boundary at 173 mbsf and the geomagnetic Matuyama/Gauss boundary at 216 mbsf (Shipboard Scientific Party, 1999c). Ages of these stratigraphic markers are, respectively, 2–2.1 Ma and 2.6 Ma (Cande and Kent, 1995). The lower section, from 360 to 525 mbsf, corresponds to the early and late Pliocene time interval, between ~3.3 and 4.2 Ma. To compare the results, the insolation signals were also analyzed on these two segments.

Some representative frequency maps are presented for the upper section in Figures F9 and F13, and the main wavenumbers and their corresponding periods are tabulated in Table T3. Note that a drastic change of SR occurs in this first segment: above 215.85 mbsf, the SR averages 8.9 cm/k.y. and below 215.85 mbsf, 20.1 cm/k.y. (Fig. F5).

The 41-k.y. period is present on the spectral map of December insolation signal (Fig. F9A). The map also reveals very strong wavenumbers: from 95 to 235 mbsf, 0.474, 0.500, and 0.592 cycles/m; and from 180 to 325 mbsf, 0.210, 0.218, and 0.264 cycles/m (Fig. F9A). These wavenumbers correspond to the Milankovitch 19- and 23-k.y. cycles (precession). As mentioned in the previous section, the wavenumbers appear to be smeared because of the high wavenumber resolution. Consequently, we list in Table T2 the limit at 216 mbsf (Fig. F7A), instead of 235 mbsf (Fig. F9A). The processing of the truncated signal contains the previous near-Milankovitch periods, especially the main precession periods with very high amplitudes, but also reveals others with significant amplitude (Fig. F9B; Table T3). The discrepancies between the periods evidenced in the signals and the primary Milankovitch periods (e.g., 22 instead of 23 k.y., or 95 instead of 100 k.y.) certainly come from the uncertainty of  $\pm 0.008$  cycles/m. Contrary to the spectral map for December insolation, the 100-k.y. period is present on the spectral map for December truncated insolation. We also observe periods different from those of Milankovitch, though much weaker (Fig. F9B; Table T3): 7, 10, 11, 12, 15, and 55 k.y. Figure F9C shows that for the reflectance signal the main wavenumbers (with high modulus, represented by the yellow and green colors) approximate all the dominant cycles in the Milankovitch band (19-, 23-, 41-, and 100-k.y. periods), particularly around 100 k.y., but

F13. Porosity, natural gamma ray, and uranium logs, Hole 1096C, p. 34.



also other periods, very close to the ones already seen in the truncated insolation between 270 and 325 mbsf: 7, 11, 13, and 48 k.y. (Table T3).

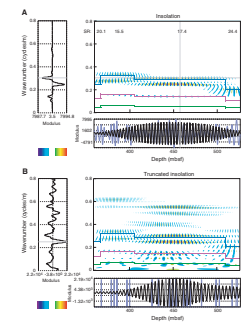
Figure F13 shows the maps for three of the logs: porosity, natural gamma ray, and uranium. As for Hole 1095B, the logs acquired in Hole 1096C do not resolve the high wavenumbers. We also note that the periods differ quite markedly from one map to another. In particular, between 95 and 270 mbsf, the strong 79- or 178-k.y. periods identified in the porosity map (Fig. F13A) are absent from the two others (Fig. F13B, F13C; Table T3). However, other periods directly related to Milankovitch cyclicities can be recognized. The near-100-k.y. cycle is present in all the results over the whole interval, although it has various amplitudes depending on the considered log (Table T3). It is also difficult to say whether or not the amplitude becomes lower with depth; for example, the amplitude for the truncated insolation analysis increases with depth, whereas it decreases sharply for the gamma ray (Fig. F13B, F13C; Table T3). Again, there is a good correlation for the 50- to 55-k.y. cycles, and this time the intensities are coherent, being rather high for all the logs. Contrary to the previous results (Fig. F9), the 23- and 41-k.y. periods are not consistent, for they appear only in the uranium map (for the precession cycle) (Fig. F13C) and in the gamma ray map (for the obliquity cycle) (Fig. F13B).

As for the previous section (95–325 mbsf), some representative frequency maps are presented for the lower section (360–525 mbsf) in Figures F14 and F15, and the main wavenumbers and their corresponding periods are tabulated in Table T4. For this second interval, the SR is fairly constant and varies between 15.5 and 24.4 cm/k.y. (Fig. F5).

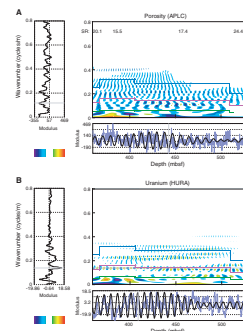
Again, the Milankovitch 19- and 23-k.y. cycles, related to precession, dominate the spectral map of December insolation signal (Fig. F14A). The 41-k.y. period (obliquity) is still present, with a much lower intensity. As for the upper section, the processing of the truncated signal contains the previous Milankovitch periods but also reveals others with significant amplitude (Fig. F14B; Table T4). For some wavenumbers, two periods are mentioned in Table T4 if their amplitudes are approximately equal across different sedimentation rates. If one period is dominant, we favored the SR corresponding to this interval to convert wavenumbers to periods. The 100-k.y. period shows up on the spectral map for December truncated insolation, and the 41-k.y. cyclicity is enhanced. As for the upper section, we also observe periods different from those of Milankovitch with various strengths (Fig. F14B; Table T4): 10, 11, 14, 16, 33, and 37 k.y.

Figure F15 shows the maps for two different logs: porosity and uranium. For this section, the wavenumber content of the uranium log, which is more complex than that for the upper section (Tables T2, T3), approximates all the dominant cycles in the Milankovitch band (19-, 23-, 41-, and 100-k.y. periods). Some of them are also found in the porosity log, though it is less clear than for the uranium log. The correlation between the various intensities is, however, poor. For example, the 19-k.y. cyclicity is highly represented in the porosity log, whereas it is quite weak in the uranium log (Table T4). The near-100-k.y. cycle is found consistently in all the results with a weak intensity, contrary to the near-41-k.y. cycle (Table T4). This period appears at 430 mbsf for the porosity log analysis, whereas it disappears at 480 mbsf for the uranium log analysis. Again, the 74- and 78-k.y. periods, near the 79-k.y. cycle mentioned above for the upper section, and the 33- and 35-k.y. periods are found in all the results with medium intensities. The 55-k.y. cycle shows up, as well as a near-61-k.y. cycle, but not in both logs.

F14. December insolation and truncated insolation, Hole 1096C, p. 36.



F15. Porosity, and uranium logs, Hole 1096C, p. 37.



It is clear that the correlation for the values of all the periods is not possible for the previous results concerning the two sections. Nevertheless, some cycles appear to be dominant in most of the signals. For example, the dominant wavenumbers for the upper section clearly change within the interval 170–270 mbsf (~2.1–2.8 Ma) for all the treated signals (Figs. F9, F13; Table T3). This interval exactly corresponds to a major unconformity between the biostratigraphic data and the geomagnetic reversals. Moreover, this change begins at the transition between lithologic Unit II and Unit III (173 mbsf). Above this transition, in Unit II, near-100-k.y. cycles appear to dominate most of the records (Figs. F9, F13; Table T3). Some signals also exhibit ~41-k.y. and 50- to 55-k.y. periods with high amplitudes. Within the transition interval, the maps show a more complex pattern of the periods, and the results are not well correlated, except for the ~23-k.y. period that appears in the truncated insolation and the gamma ray measurements (Table T3). Below the transition, near-100-k.y. cycles appear again in all the maps (Figs. F9, F13), but, whereas it is the dominant period for the truncated insolation, reflectance, and uranium, the amplitude is much lower for the porosity or natural gamma ray (Table T3). For this lower section, all the maps reveal ~41-k.y. and 50- to 55-k.y. periods with strong amplitudes, whereas the 23-k.y. cycles are only seen in the truncated insolation (dominant period) and in the uranium and reflectance signals with much weaker amplitude. This gradual shift near 2.5 Ma is consistent with discontinuities evidenced in other studies reflecting significant climate changes. For example, a large discontinuity at 3 Ma was evidenced in the oxygen isotope ratios in Atlantic benthic foraminifers (Barker et al., 1999). This 2.5-Ma shift was also pointed out by DeMenocal et al. (1991) in the Arabian Sea, even if the pattern expressed here is different. For the drift Site 1096, this shift probably reflects a change in sediment input related to the history of channel development on either side of the drift, development driven by alternation of glacial–interglacial periods (e.g., Shipboard Scientific Party, 1999a); a northeastern channel, which did not exist for much of Unit III time, was perhaps reactivated, leading to distal turbidites in Unit II.

The differences between the upper and lower section periods (e.g., for the porosity log, 110 instead of 106 k.y. or 55 instead of 52 k.y.) can be explained by uncertainties in the age model and discrepancies in depth position, as the logs were recovered during two separate runs. The main cycles present in the insolation signals for the lower section are 19 and 23 k.y. (precession) with the maximum of amplitude between 400 and 450 mbsf (Fig. F14). The 41- and 100-k.y. cycles are also recognized with medium amplitude. Most of the periods appear to be highly variable in intensity, the contribution of the different periods being either amplified or lowered near 400/450 mbsf (Figs. F14, F15). Some of them disappear or appear at ~450 mbsf, or the intensity diminishes drastically between 400 and 450 mbsf. This limit is coherent with a change in the core observation (Shipboard Scientific Party, 1999c): above 450 mbsf, the laminated silty clay facies dominates, whereas below 450 mbsf, the sediments are mostly massive, bioturbated, more biogenic sandy silty clays. This interval from 3.5 to 3.8 Ma, therefore, appears to be a major change in the sediment supply induced by climate changes, as also evidenced by Weber (submitted [N1]) in the eastern equatorial Pacific.

Although it seems that the sedimentary cyclicity at Site 1096 may have some orbital forcing, other anomalous periods, which do not correspond to primary Milankovitch periods, are also revealed, such as the

50- to 55-k.y. period that is known to be related to eccentricity (e.g., Imbrie and Imbrie, 1979; Imbrie, 1985). In the lower section (Pliocene), a new cycle appears around 33–35 k.y. This period might be related to the 30- to 35-k.y. periods commonly found in Pliocene to Pleistocene eolian time series (Rea, 1994; Lauer-Leredde et al., 1998). Such periods could result from nonlinear responses of the climate system to orbital forcing, most probably interferences of precession and obliquity. We also record periods around 74/80 k.y. for the early Pleistocene and late Pliocene time intervals. These approximate a major peak at 78 k.y. recorded by Robinson (1990) from middle and lower Pleistocene in the tropical Indian Ocean. Ghil (1987) and Robinson (1990) first suggested it might be harmonic or combination tones that reflect nonlinear interactions between primary Milankovitch periods. Transitional states, which have most of their power at a period of ~75 k.y., were also evidenced by Bolton et al. (1995) in climatic records derived from oxygen isotopic ratios of Pliocene–Pleistocene marine sediment cores at ODP Site 677. Liu and Chao (1998) explained an ~80-k.y. cycle, which briefly appeared in the Pleistocene, as a multiple of the obliquity and precession periods. For them, this cycle evolved into the 100-k.y. cycle, these flickers being induced by the amplitude variation of obliquity and precession.

## CONCLUSIONS

We used wavelets to analyze the frequency content of core and log measurements from upper Miocene to Pleistocene drift sediments located west of the Antarctic Peninsula. To assess the reliability of our results and their relation to insolation, we also analyzed insolation and truncated insolation signals transformed to the depth scales of Holes 1095B and 1096C. We found that accurate dating of the cores and logs is very important for accurate determination of the dominant frequencies, and hence for the climatic information implied by those frequencies. Our results show that wavelet transform analysis can be useful for the stratigraphic interpretation of core and log measurements.

Some main results that relate to the understanding of the glacial history of the Antarctic Peninsula can be highlighted:

1. A few of the log and core measurements vary with periods close the Milankovitch periods, not only in the Pliocene–Pleistocene, but also in the Miocene. For example, a persistent ~100-k.y. cycle (with variable amplitude) is present in some the wavelet transforms for the Pliocene–Pleistocene period.
2. Periods different from those of Milankovitch are revealed, such as 30–35, 50–55, and 74–78 k.y. Similar periods have been observed by other authors for the same time interval (Imbrie and Imbrie, 1979; Imbrie, 1985; Ghil, 1987; Robinson, 1990; Rea, 1994; Bolton et al., 1995; Lauer-Leredde et al., 1998).
3. Discontinuities in the frequency content of the log and core measurements are recognized in the depth-wavenumber maps. A change is observed during the late Miocene, at ~8 Ma, giving rise to dominantly shorter periods until 7.5 Ma. It is important to note that this pattern correlates with higher sedimentation rates, whatever the considered age models. The Pleistocene–Pliocene interval also exhibits two dominant shifts: the first near 2.1–2.8 Ma and the second near 3.5–3.8 Ma. This is consistent with

changes in lithology and climatic transitions elsewhere on the globe (Liu and Chao, 1998).

## **ACKNOWLEDGMENTS**

The authors wish to acknowledge the contribution of Olivier Voutay and especially Mohamed Ramadan (presently at Techsia Company, Montpellier-France), who helped us write the software Statilog used for this study. We also wish to thank D. Barthes for the use of the wavelet transform code he developed and for his advice. We also thank the reviewers and G. Acton for their comments and invaluable suggestions.

This research used samples and/or data provided by the Ocean Drilling Program (ODP). ODP is sponsored by the U.S. National Science Foundation (NSF) and participating countries under management of Joint Oceanographic Institutions (JOI), Inc.

## REFERENCES

- Barker, P.F., Barrett, P.J., Cooper, A.K., and Huybrechts, P., 1999. Antarctic glacial history from numerical models and continental margin sediments. *Palaeogeogr., Palaeoclimatol., Palaeoecol.*, 150:247–267.
- Barthes, D., and Mattei, J.A., 1997. Time-frequency analysis and pulsation modes of LVP stars. *I.O. Ceti. Astron. J.*, 113:373–390.
- Berger, A., 1976. Obliquity and precession for the last 5,000,000 years. *Astron. Astrophys.*, 51:127–135.
- Berger, A.L., 1978. Long-term variations of daily insolation and quaternary climatic changes. *J. Atmos. Sci.*, 35:2362–2367.
- Berger, A., Loutre, M.F., and Dehant, V., 1989. Influence of the changing lunar orbit on the astronomical frequencies of the Pre-Quaternary insolation patterns. *Paleoceanography*, 4:555–564.
- Bolton, E.W., Maasch, K.A., and Lilly, J.M., 1995. A wavelet analysis of Plio–Pleistocene climate indicators: a new view of periodicity evolution. *Geophys. Res. Lett.*, 22:2753–2756.
- Bretagnon, P., 1974. Termes à longues périodes dans le système solaire. *Astron. Astrophys.*, 30:141–154.
- Cande, S.C., and Kent, D.V., 1995. Revised calibration of the geomagnetic polarity timescale for the Late Cretaceous and Cenozoic. *J. Geophys. Res.*, 100:6093–6095.
- Carmona, R., Hwang, W.L., and Torrésani, B., 1998. *Practical Time-Frequency Analysis. Gabor and Wavelet Transform with Implementation in Science*: New York (Academic Press).
- deMenocal, P., Bloemendal, J., and King, J., 1991. A rock-magnetic record of monsoonal dust deposition to the Arabian Sea: evidence for a shift in the mode of deposition at 2.4 Ma. In Prell, W.L., Niitsuma, N., et al., *Proc. ODP, Sci. Results*, 117: College Station, TX (Ocean Drilling Program), 389–407.
- Ellis, D.V., 1987. *Well Logging for Earth Scientists*: New York (Elsevier).
- Foufoula-Georgiou, E., and Kumar, P. (Eds.), 1995. *Wavelets in Geophysics*: New York (Academic Press).
- Ghil, M., 1987. Nonlinear phenomena in climate dynamics. In Nicolis, C., and Nicolis, G. (Eds.), *Irreversible Phenomena and Dynamical Systems Analysis in Geosciences*. NATO ASI, Ser. C, 194:313–320.
- Goupillaud, P., Grossmann, A., and Morlet, J., 1984. Cycle-octave and related transforms in seismic signal analysis. *Geoexploration*, 23:85–102.
- Grossman, A., and Morlet, J., 1984. Decomposition of Hardy functions into square integrable wavelets of constant shape. *SIAM J. Math. Anal.*, 15:723–736.
- Imbrie, J., 1985. A theoretical framework for the Pleistocene ice ages. *J. Geol. Soc. London*, 142:417–432.
- Imbrie, J., and Imbrie, K.P., 1979. *Ice Ages: Solving the Mystery*: Short Hills, N.J. (Enslow Publications).
- Kumar, P., and Foufoula-Georgiou, E., 1997. Wavelet analysis for geophysical applications. *Rev. Geophys.*, 35:385–412.
- Laskar, J., 1988. Secular evolution of the solar system over 10 million years. *Astron. Astrophys.*, 198:341–362.
- , 1990. The chaotic motion of the solar system: a numerical estimate of the size of the chaotic zones. *Icarus*, 88:266–291.
- , 1993. Orbital, precessional, and insolation quantities for Earth from –20 Myr to +10 Myr. *Astron. Astrophys.*, 270:522–533.
- , 1999. The limits of Earth orbital calculations for geological time-scale use. *Philos. Trans. R. Soc. London, Ser. A*, 357:1735–1759.
- Lauer-Leredde, C., Pezard, P., Robert, C., and Dekeyser, I., 1998. Mineralogical association and physical properties of sediments with palaeoclimatic implications (ODP

- Site 798, Japan Sea): a comparative study from core and downhole measurements. *Mar. Geol.*, 150:73–98.
- Liu, H.S., and Chao, B.F., 1998. Wavelet spectral analysis of the Earth's orbital variations and paleoclimatic cycles. *J. Atmos. Sci.*, 55:227–236.
- McGinnis, J.P., and Hayes, D.E., 1995. The roles of downslope and along-slope depositional processes: southern Antarctic Peninsula continental rise. In Cooper, A.K., Barker, P.F., and Brancolini, G. (Eds.), *Geology and Seismic Stratigraphy of the Antarctic Margin*. Am. Geophys. Union, Antarct. Res. Ser., 68:141–156.
- Meyer, Y. (Ed.), 1992. *Wavelets and Applications: Proc. Int. Conf., Marseille, France, May 1989*. Paris (Springer Verlag).
- Morlet, J., Arens, G., Fourgeau, E., and Giard, D., 1982a. Wave propagation and sampling theory, 1. Complex signal and scattering in multilayered media. *Geophysics*, 47:203–221.
- , 1982b. Wave propagation and sampling theory, 2. Sampling theory and complex waves. *Geophysics*, 47:222–236.
- Rea, D.K., 1994. The paleoclimatic record provided by eolian deposition in the deep sea: the geologic history of wind. *Rev. Geophys.*, 32:159–195.
- Rebesco, M., Camerlenghi, A., and Zanolla, C., 1998. Bathymetry and morphogenesis of the continental margin west of the Antarctic Peninsula. *Terra Antart.*, 5:715–728.
- Rebesco, M., Larter, R.D., Barker, P.F., Camerlenghi, A., and Vanneste, L.E., 1997. The history of sedimentation on the continental rise west of the Antarctic Peninsula. In Barker, P.F., and Cooper, A.K. (Eds.), *Geology and Seismic Stratigraphy of the Antarctic Margin* (Pt. 2). Am. Geophys. Union, Antarctic Res. Ser., 71:29–50.
- Rebesco, M., Larter, R.D., Camerlenghi, A., and Barker, P.F., 1996. Giant sediment drifts on the continental rise of the Antarctic Peninsula. *Geo-Mar. Lett.*, 16:65–75.
- Robinson, S.G., 1990. Applications for whole-core magnetic susceptibility measurements of deep-sea sediments: Leg 115 results. In Duncan, R.A., Backman, J., Peterson, L.C., et al., *Proc. ODP, Sci. Results*, 115: College Station, TX (Ocean Drilling Program), 737–771.
- Serra, O., 1979. Diagraphies différées; bases de l'interprétation, Tome 1. Acquisition des données diagraphiques. *Bull. Cent. Rech. Explor.-Prod. Elf Aquitaine*, Mem. 1.
- , 1985. Diagraphies différées; bases de l'interprétation. Tome 2: Interprétation des données diagraphiques. *Bull. Centres Rech. Explor.-Prod. Elf-Aquitaine*, Mem. 7.
- Shipboard Scientific Party, 1999a. Leg 178 summary: Antarctic glacial history and sea-level change. In Barker, P.F., Camerlenghi, A., Acton, G.D., et al., *Proc. ODP, Init. Repts.*, 178: College Station TX (Ocean Drilling Program), 1–58.
- , 1999b. Site 1095. In Barker, P.F., Camerlenghi, A., Acton, G.D., et al., *Proc. ODP, Init. Repts.*, 178, 1–173 [CD-ROM]. Available from: Ocean Drilling Program, Texas A&M University, College Station, TX 77845-9547, U.S.A.
- , 1999c. Site 1096. In Barker, P.F., Camerlenghi, A., Acton, G.D., et al., *Proc. ODP, Init. Repts.*, 178, 1–144 [CD-ROM]. Available from: Ocean Drilling Program, Texas A&M University, College Station, TX 77845-9547, U.S.A.
- Torrence, C., and Compo, G.P., 1998. A practical guide to wavelet analysis. *Bull. Am. Meteorol. Soc.*, 79:61–78.

Figure F1. Bathymetric chart of the Antarctic Peninsula Pacific margin (after Rebesco et al., 1998) with Leg 178 sites marked (bathymetry in meters). SM = seamount.

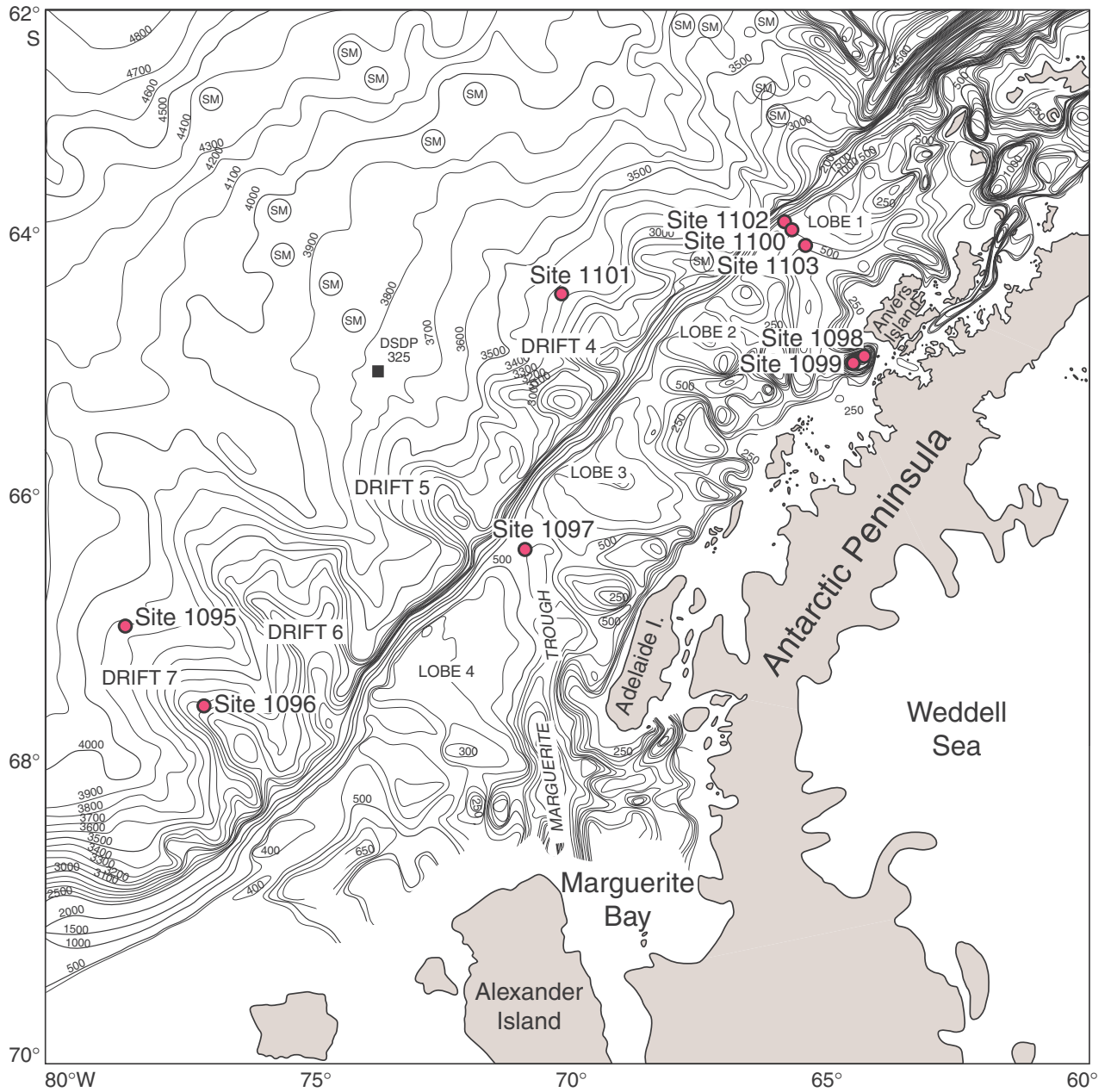
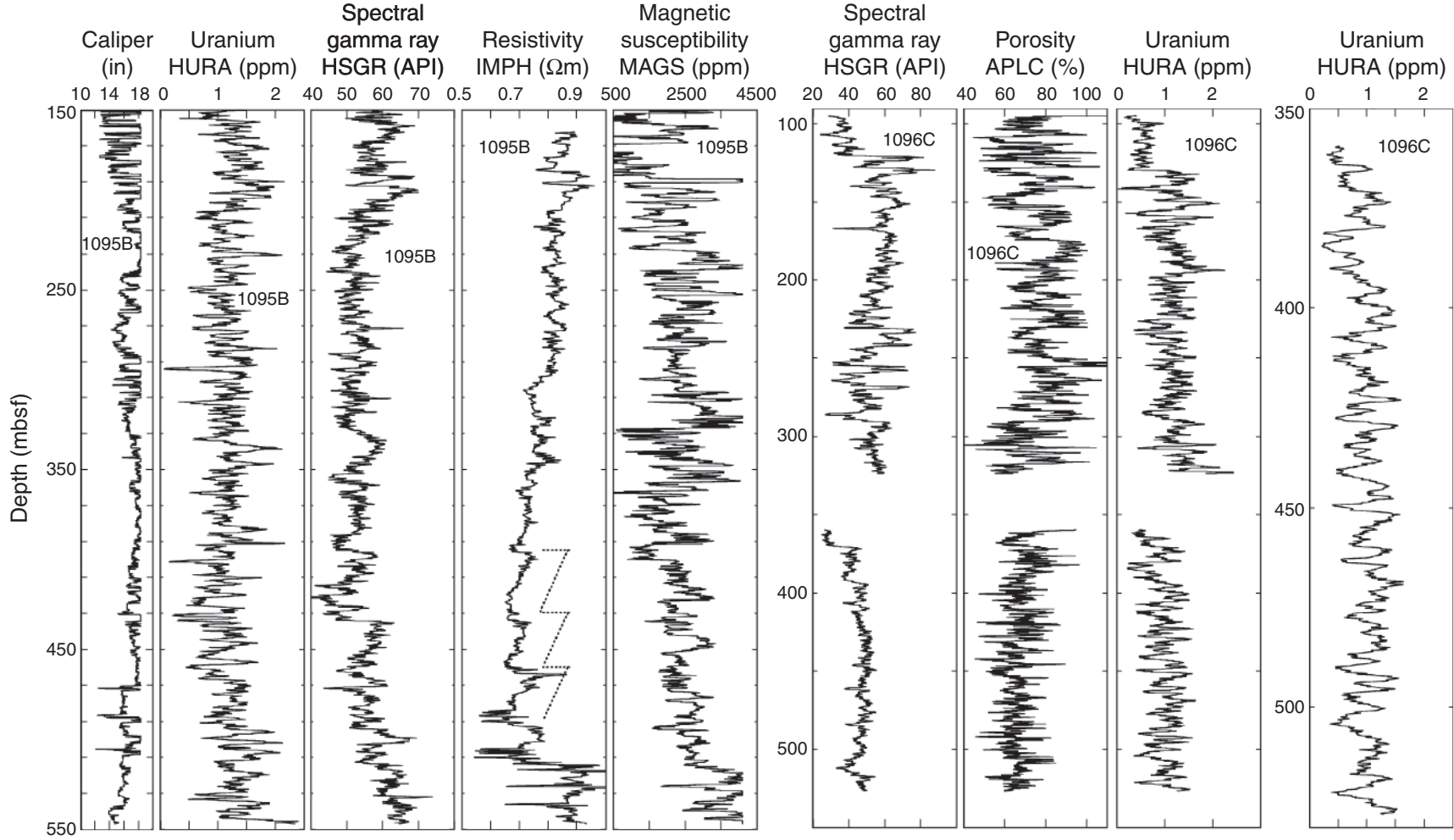


Figure F2. Main downhole measurements in Holes 1095B and 1096C. The dashed lines enhance the pattern that repeats three times.



**Figure F3.** Bioturbated interval signals extracted from the master lithostratigraphic column of Hole 1095B (see “Core Measurements,” p. 4, in “Physical Properties Data”) and raw measurements made on cores from Holes 1095B and 1096C: lightness parameter or reflectance ( $L^*$ ), natural gamma ray (NGR), and magnetic susceptibility (MAGS).

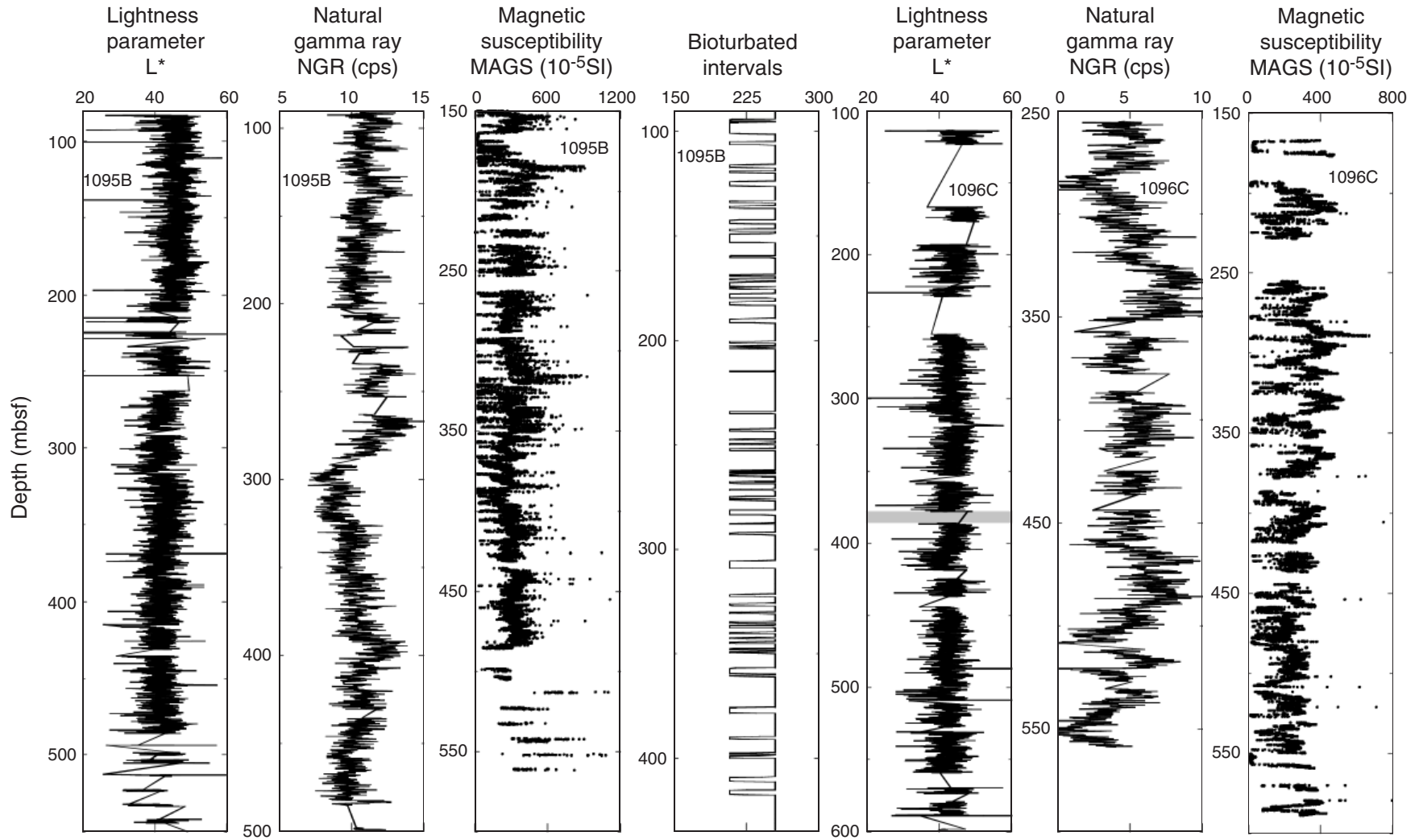


Figure F4. Insolation signals computed at 67°S with Laskar (1993, 1999) program.

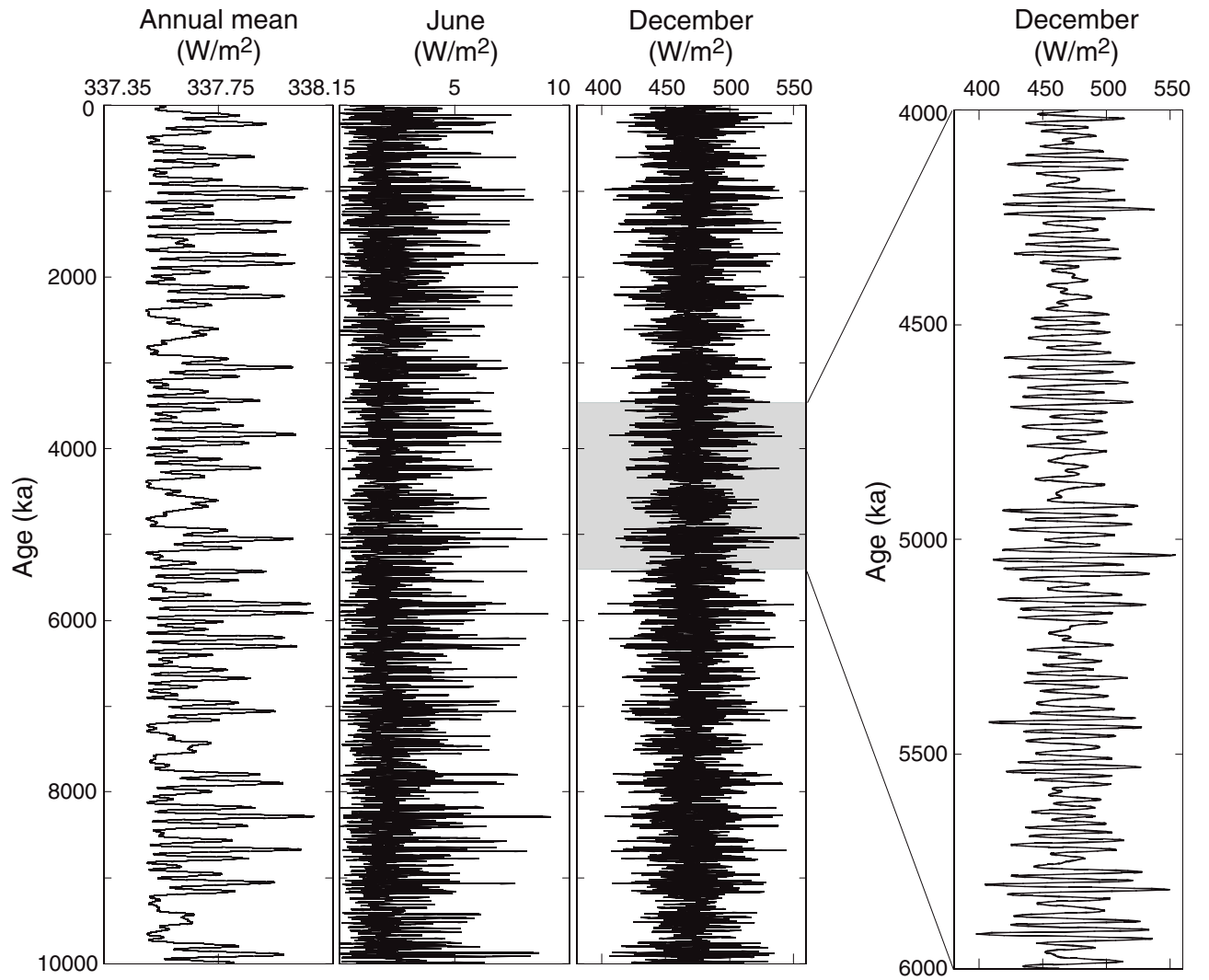


Figure F5. Sedimentation rates (SRs) vs. depth for (A) Site 1095 and (B) Site 1096. Heavy line = paleomagnetic data from the combined core and GHMT data set, dashed line = radiolarian data, gray line = diatom data.

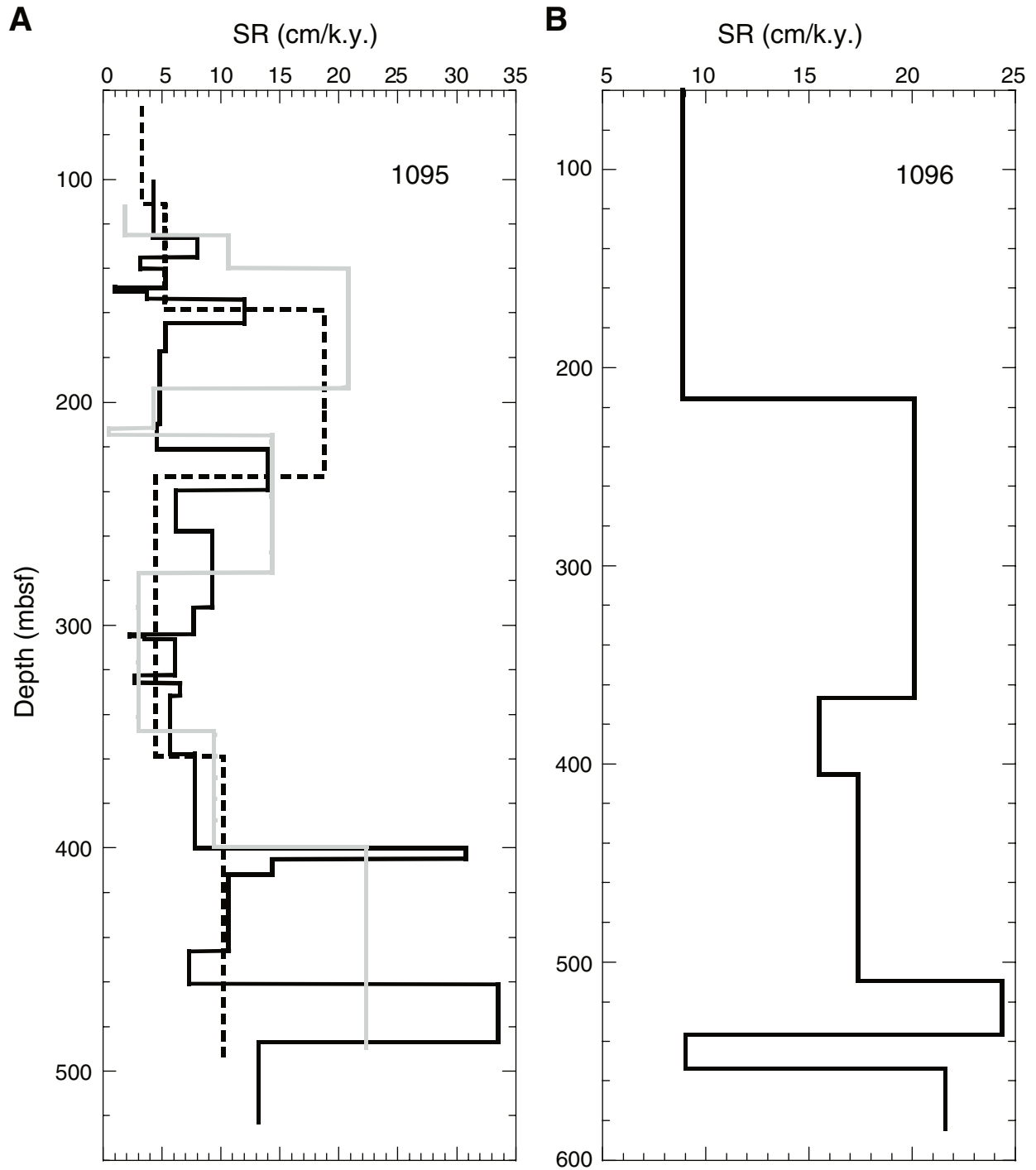
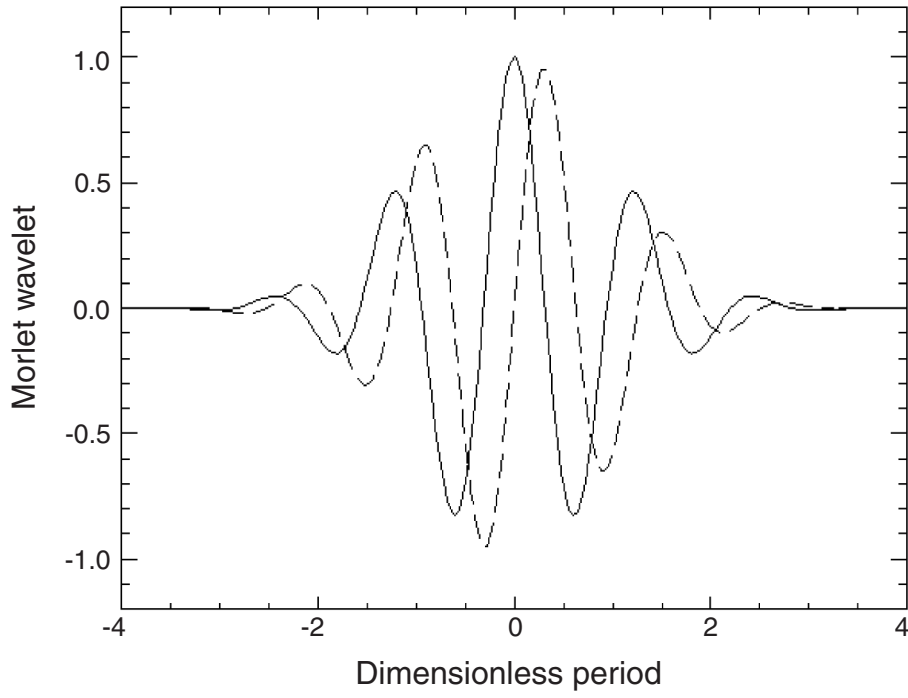


Figure F6. Real (solid line) and imaginary (dashed line) parts of the Morlet wavelet.



**Figure F7.** Spectral map for (A) the December insolation signal converted to a depth scale using Hole 1096C age model. The horizontal and vertical axis represent, respectively, the depth and the wavenumber. The color scale goes from blue (high negative modulus, which corresponds to a trough in the signal) to red (high positive modulus, which corresponds to a peak in the signal). Note that we modified the modulus color scale to eliminate the nonsignificant wavenumbers (see Torrence and Compo, 1998). For that, we attributed the white color to the low modulus absolute values. The real part is represented here. The diagrams on the left display the modulus of the wavelet transform vs. wavenumber; wavenumber for a chosen depth specified on the spectral map by a vertical gray line. The diagram under the map displays in blue the processed signal, and in black, the periodic signal for a chosen wavenumber specified on the spectral map by an horizontal gray line. On the spectral map A, the green, pink, and blue lines, respectively, represent the Milankovitch 100-, 40-, and 20-k.y. periods, computed using the age model deduced from paleomagnetic data. The frequency resolution used here for the wavelet transform is 0.01 cycles/m, instead of 0.002 cycles/m (see “[Time-Frequency Analysis Results and Discussion](#),” p. 7). (Continued on next page.)

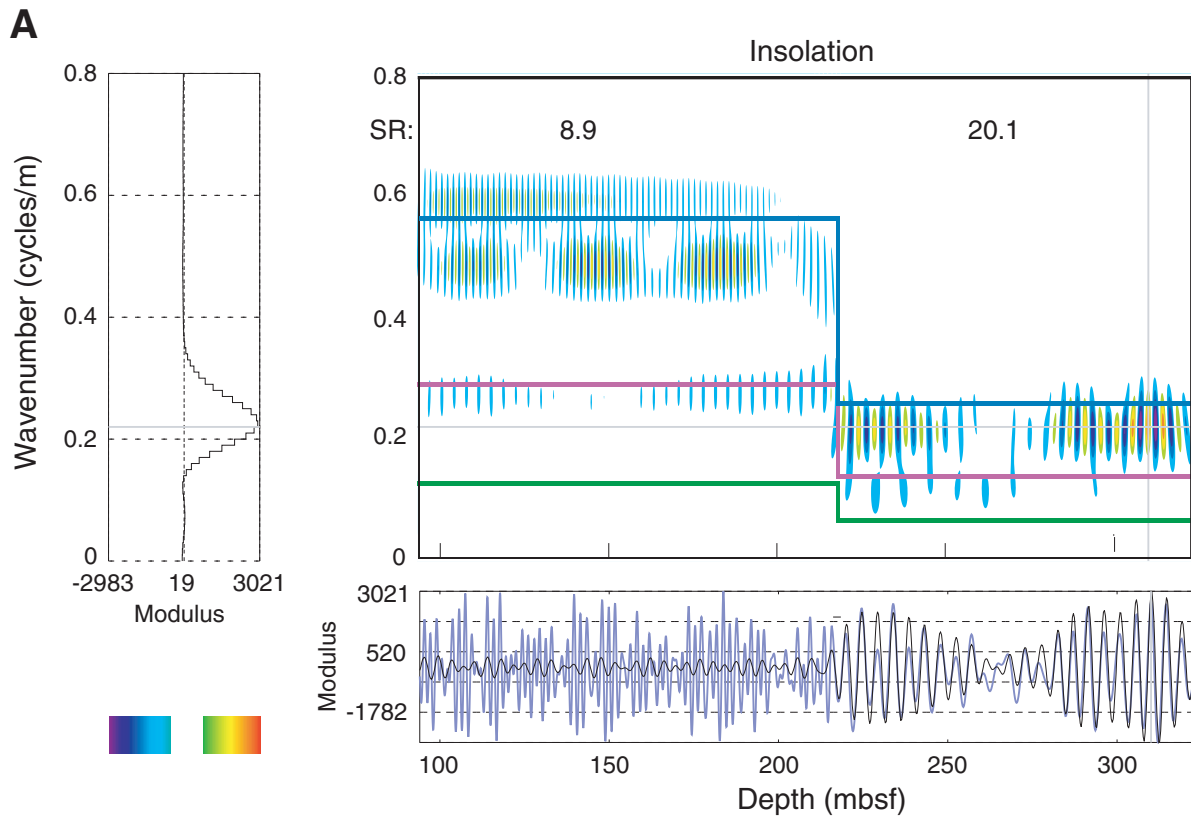


Figure F7 (continued). (B) Signal truncated at 510 W/m<sup>2</sup> and (C) core magnetic susceptibility, Hole 1095B.

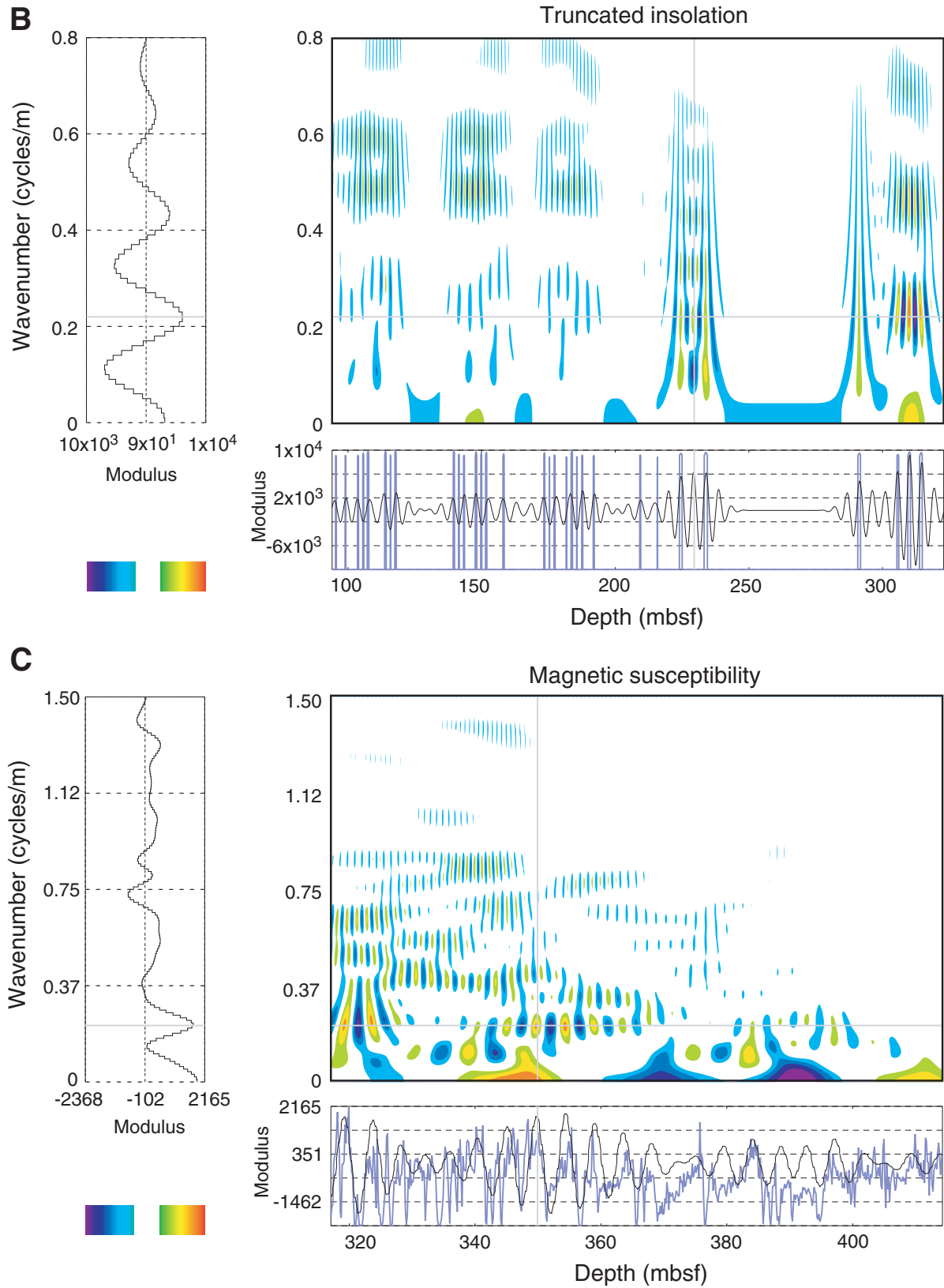


Figure F8. Hole 1095B. Spectral maps for (A) the December insolation signal truncated at  $510 \text{ W/m}^2$  and (B) the core magnetic susceptibility. The presentation is the same as Figure F7, p. 24. On the spectral map A, the green, pink, and blue lines, respectively, represent the Milankovitch 100-, 40-, and 20-k.y. periods, computed using the age model deduced from paleomagnetic data. (Continued on next page.)

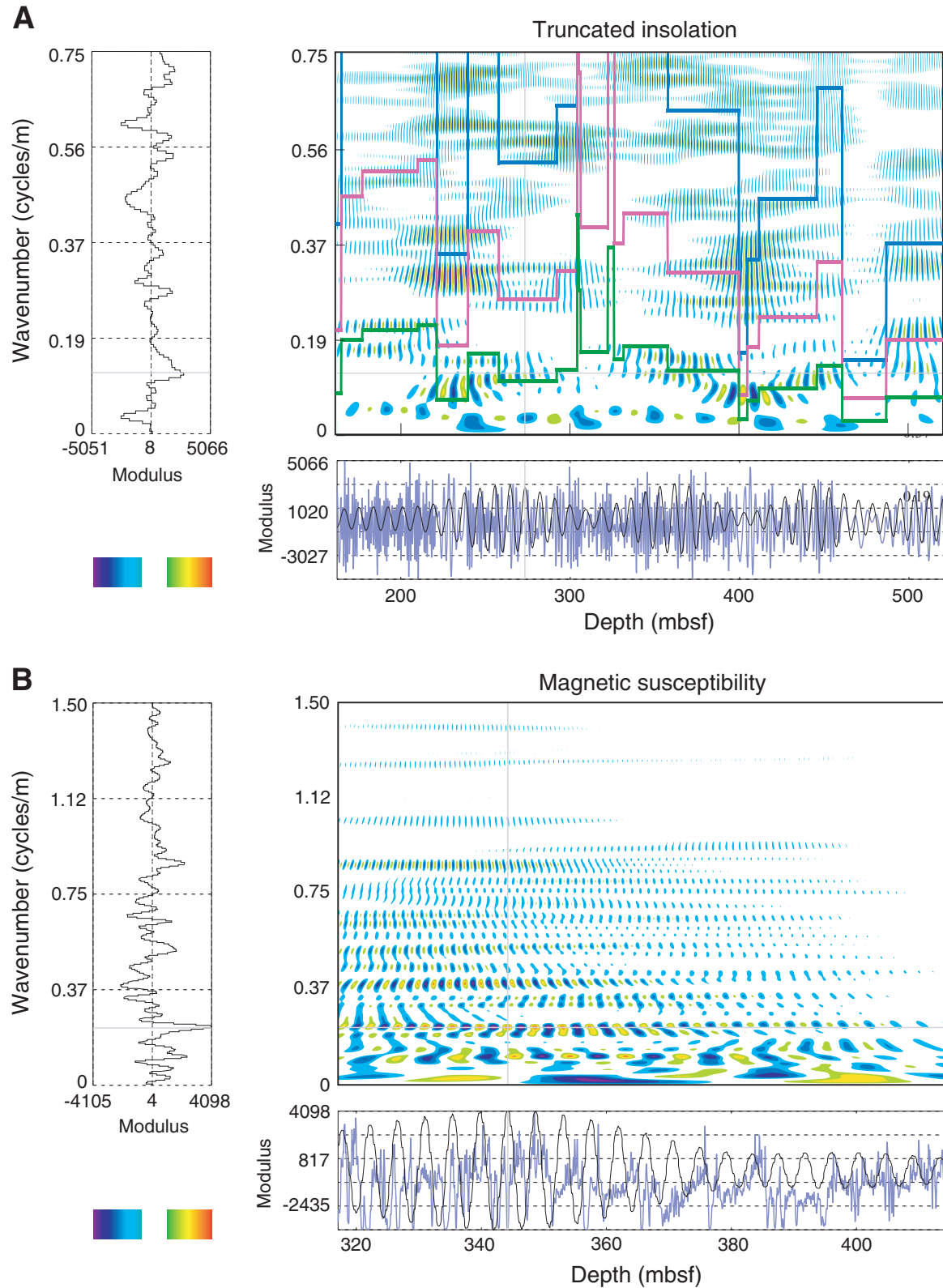


Figure F8 (continued). (C) Bioturbated intervals signal.

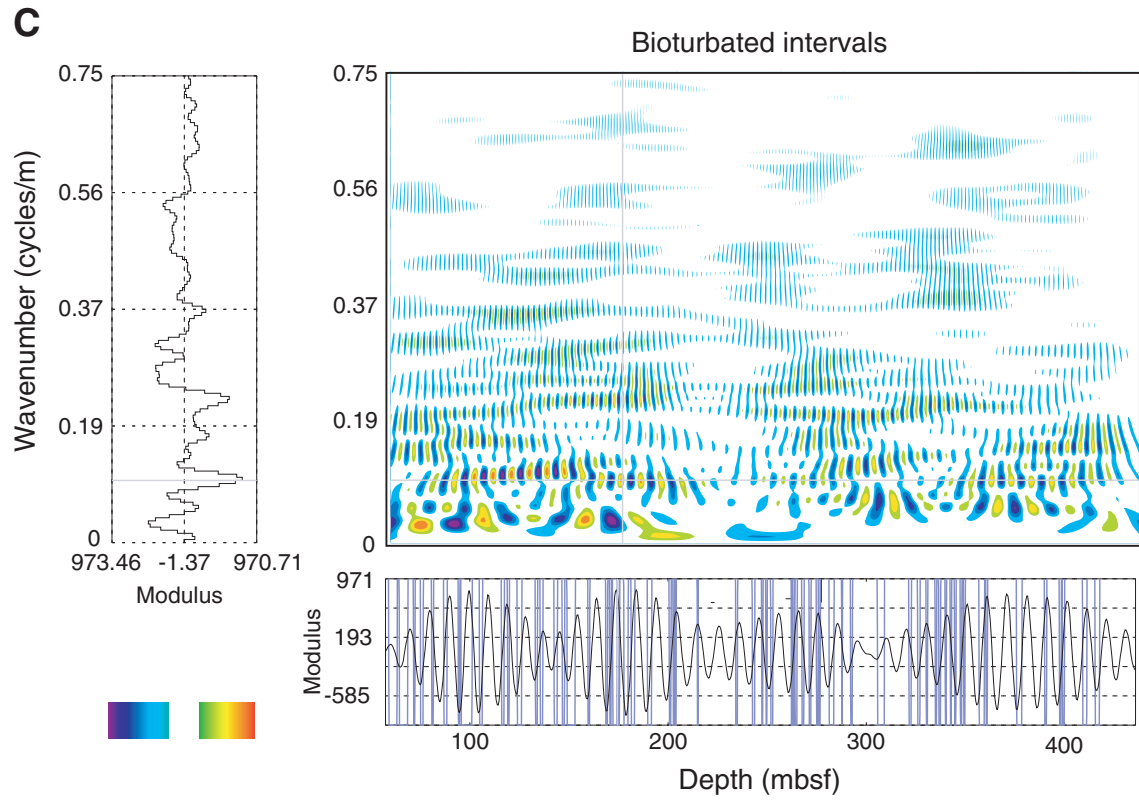


Figure F9. Hole 1096C, upper section (from 95 to 325 mbsf). Spectral maps for (A) the December insolation signal and (B) the truncated insolation signal. The presentation is the same as Figure F7, p. 24. SR = sedimentation rate. (Continued on next page.)

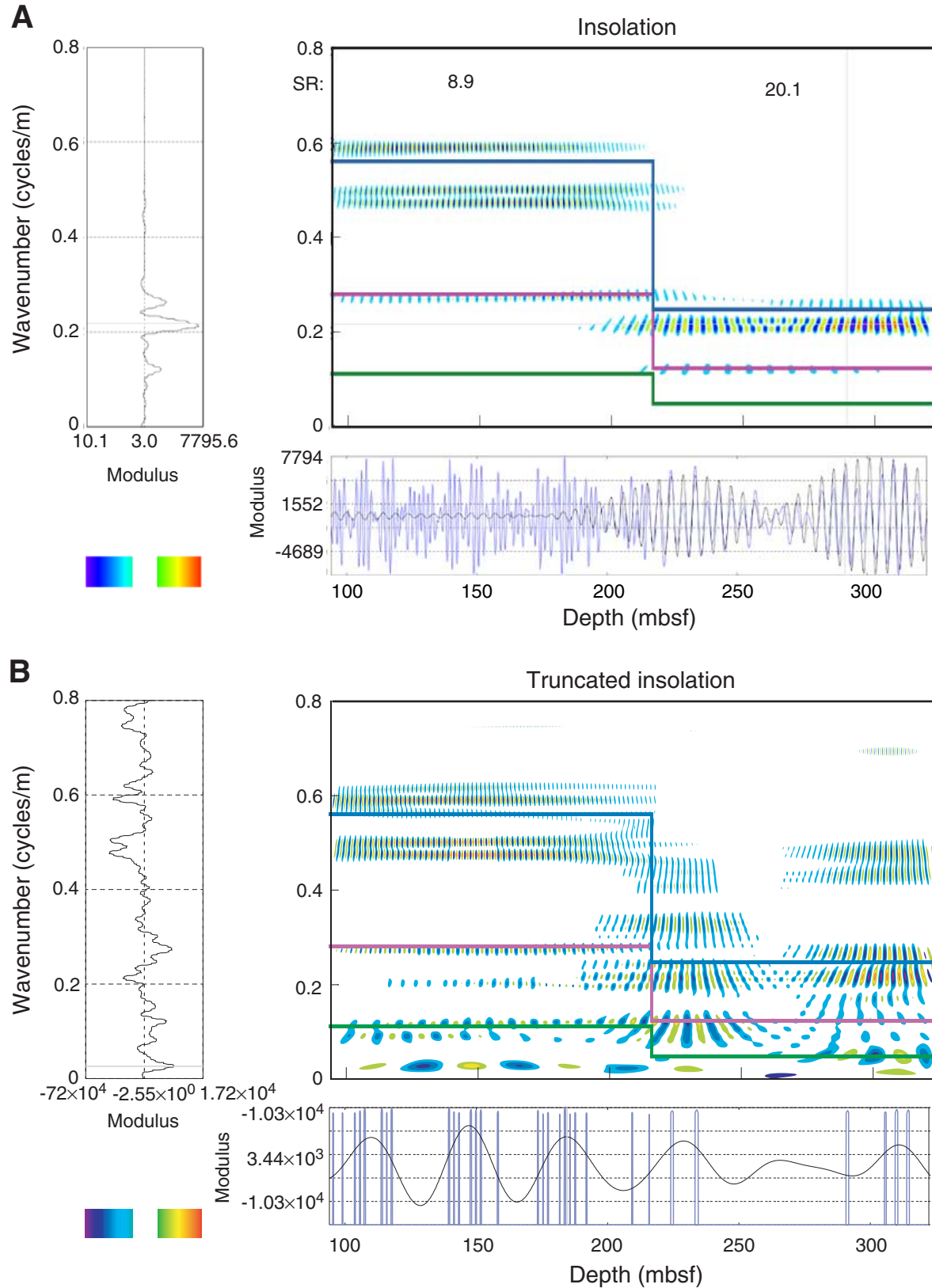
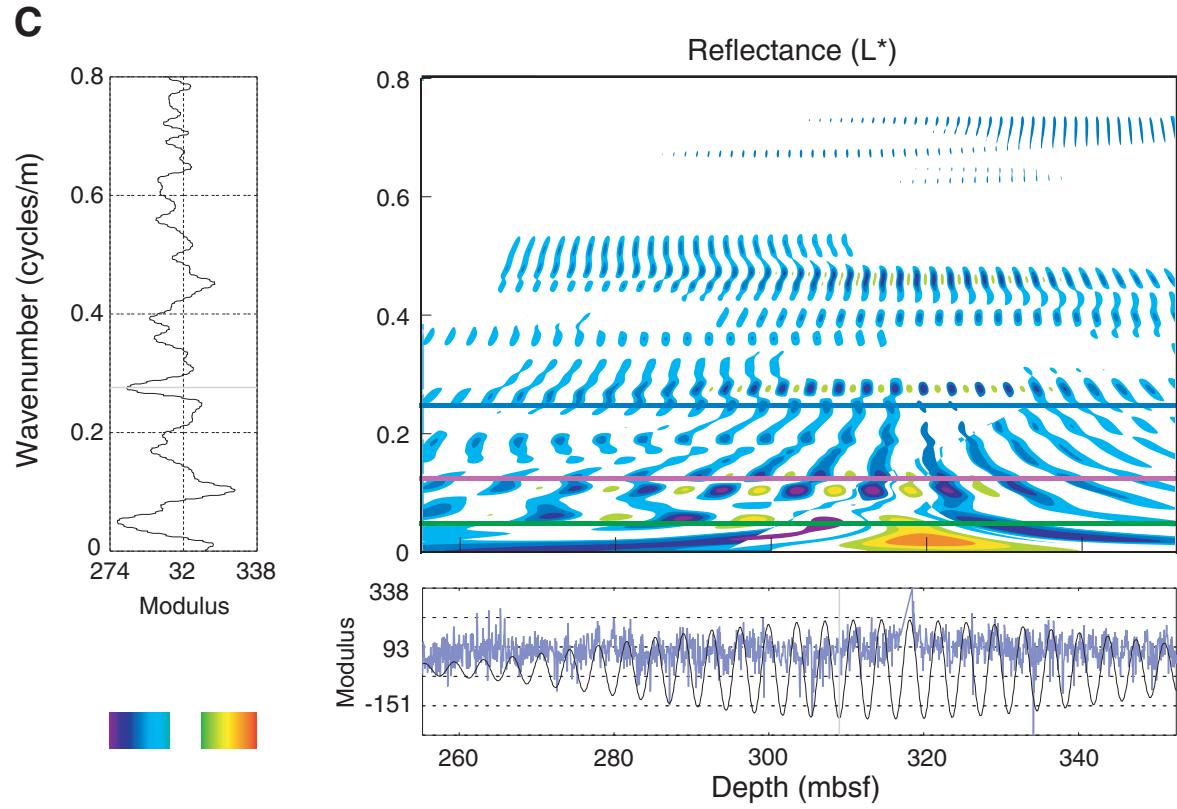
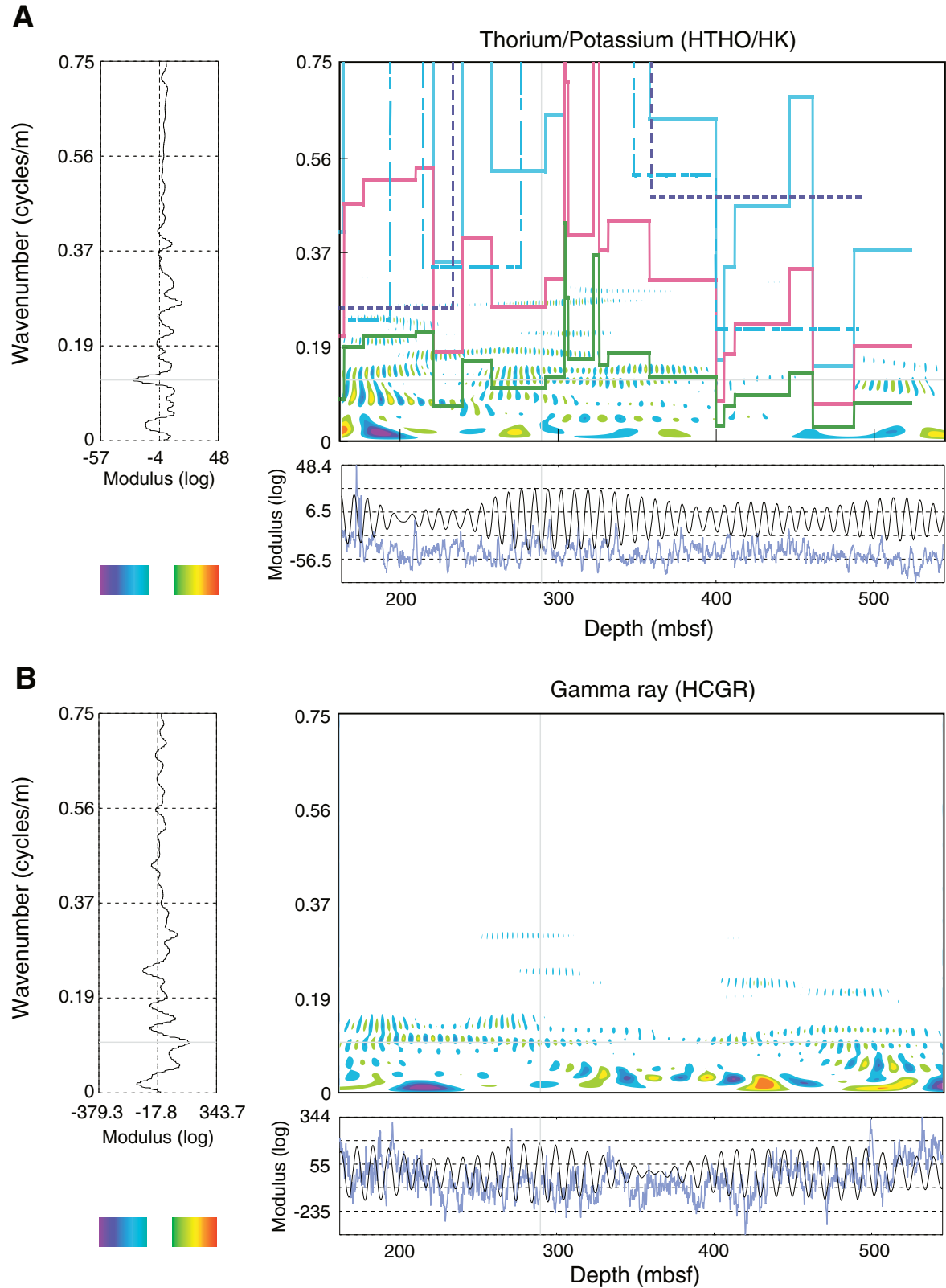


Figure F9 (continued). (C) Core reflectance measurements.



**Figure F10.** Hole 1095B. Spectral maps for (A) the thorium/potassium ratio and (B) the natural gamma ray logs. The presentation is the same as Figure F7, p. 24. On the spectral map A, the green, pink, and blue heavy lines, respectively, represent the Milankovitch 100-, 40-, and 20-k.y. periods, computed using the age model deduced from paleomagnetic data. The blue and dark blue dashed lines, respectively, represent the Milankovitch 20-k.y. period, computed using the age models deduced from diatom and radiolarian data.



**Figure F11.** Spectral map for (A) the June insolation signal. The horizontal and vertical axis represent, respectively, the age and the frequency. The color scale goes from blue (high negative modulus, which corresponds to a trough in the signal) to red (high positive modulus, which corresponds to a peak in the signal). Note that we modified the modulus color scale to eliminate the nonstatistically significant wavenumbers (see Torrence and Compo, 1998). For that, we attributed the white color to the low modulus absolute values. The modulus part is represented here. The diagrams on the left display the modulus of the wavelet transform vs. frequency; frequency for a chosen depth specified on the spectral map by a vertical gray line. The diagram under the map displays in blue the processed signal. (Continued on next page.)

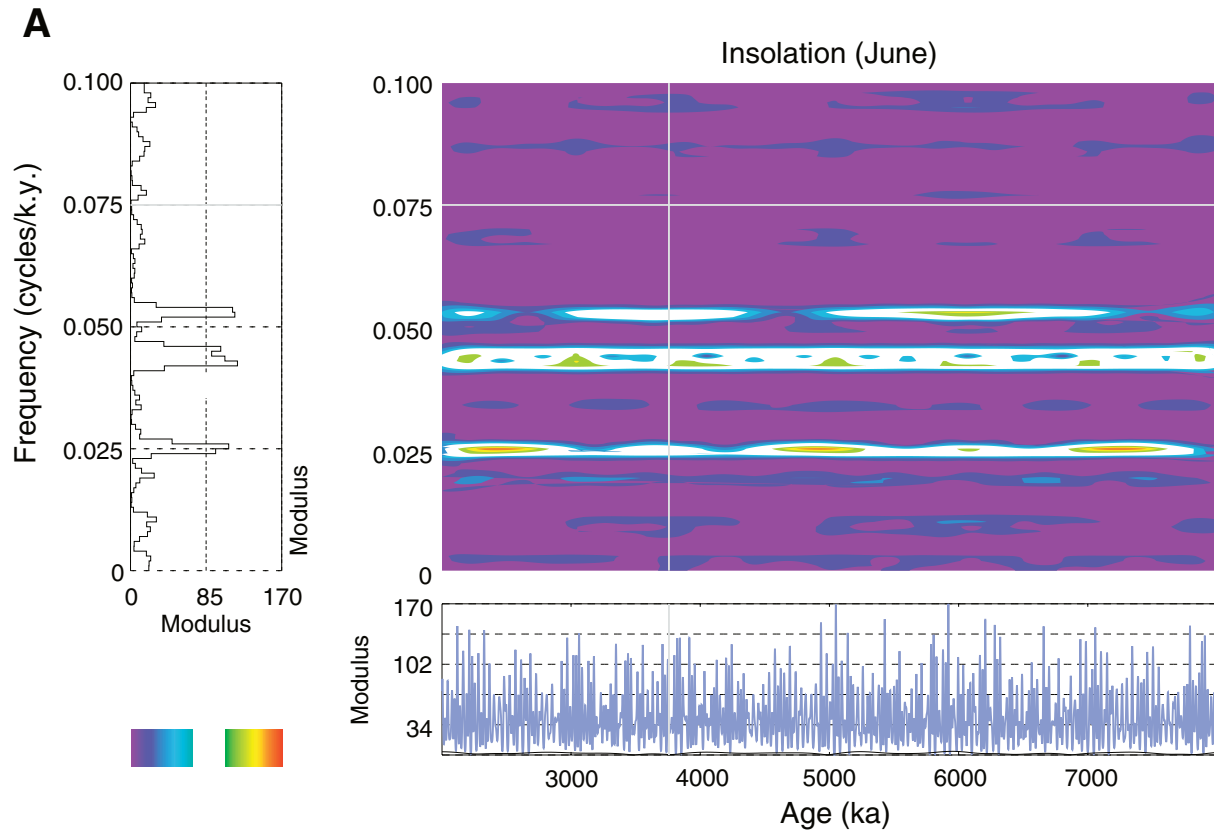


Figure F11 (continued). (B) December insolation signal and (C) insolation signal truncated at  $510 \text{ W/m}^2$ .

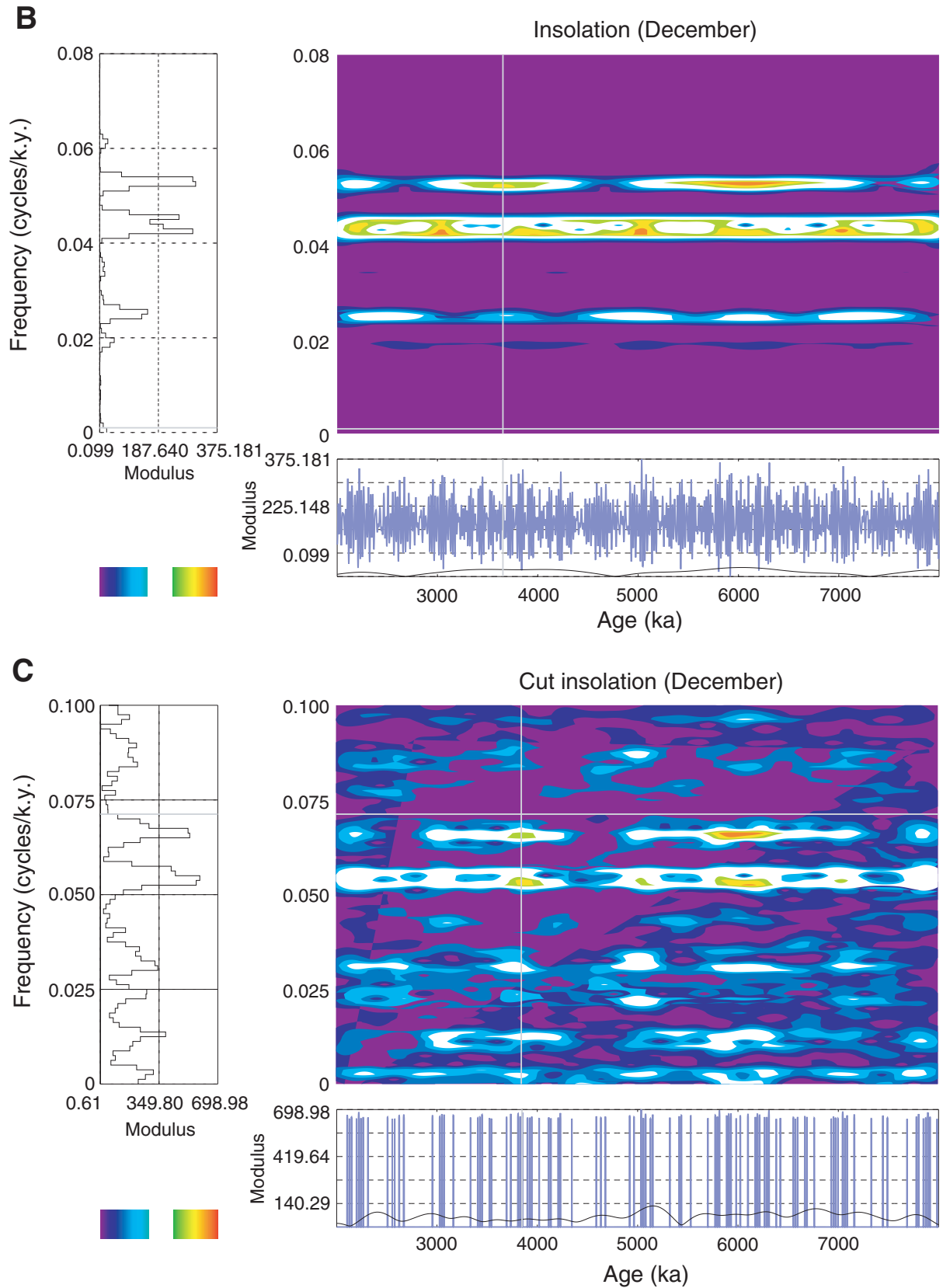


Figure F12. Hole 1095B. Synthesis combining all the results from Figures F8, p. 26, and F10, p. 30, and Table T1, p. 38. On the left, the master lithostratigraphic column of Hole 1095B shows dominant lithology (from Shipboard Scientific Party, 1999b). Black color is for bioturbated intervals, and white, for fine-grained turbidite facies. On the right, the main periods and their depth of appearance are summarized for the natural gamma ray and the thorium/potassium ratio logs (labeled CGR and Th/K), the bioturbated intervals (labeled silts), and the core magnetic susceptibility. SR = sedimentation rate, no F. = no frequency.

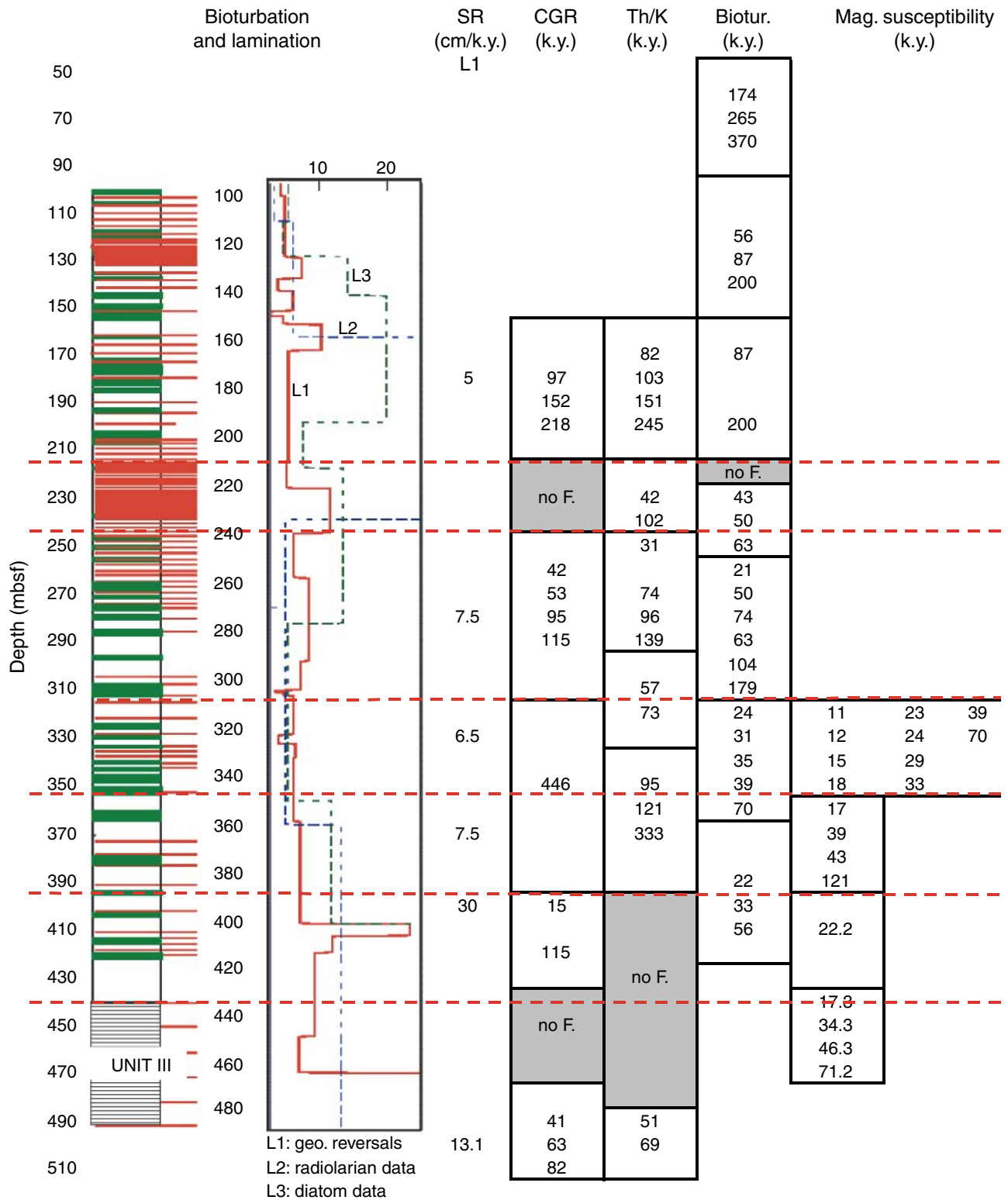


Figure F13. Hole 1096C, upper section (from 95 to 325 mbsf). Spectral maps for (A) porosity and (B) natural gamma ray logs. The presentation is the same as Figure F7, p. 24. SR = sedimentation rate. (Continued on next page.)

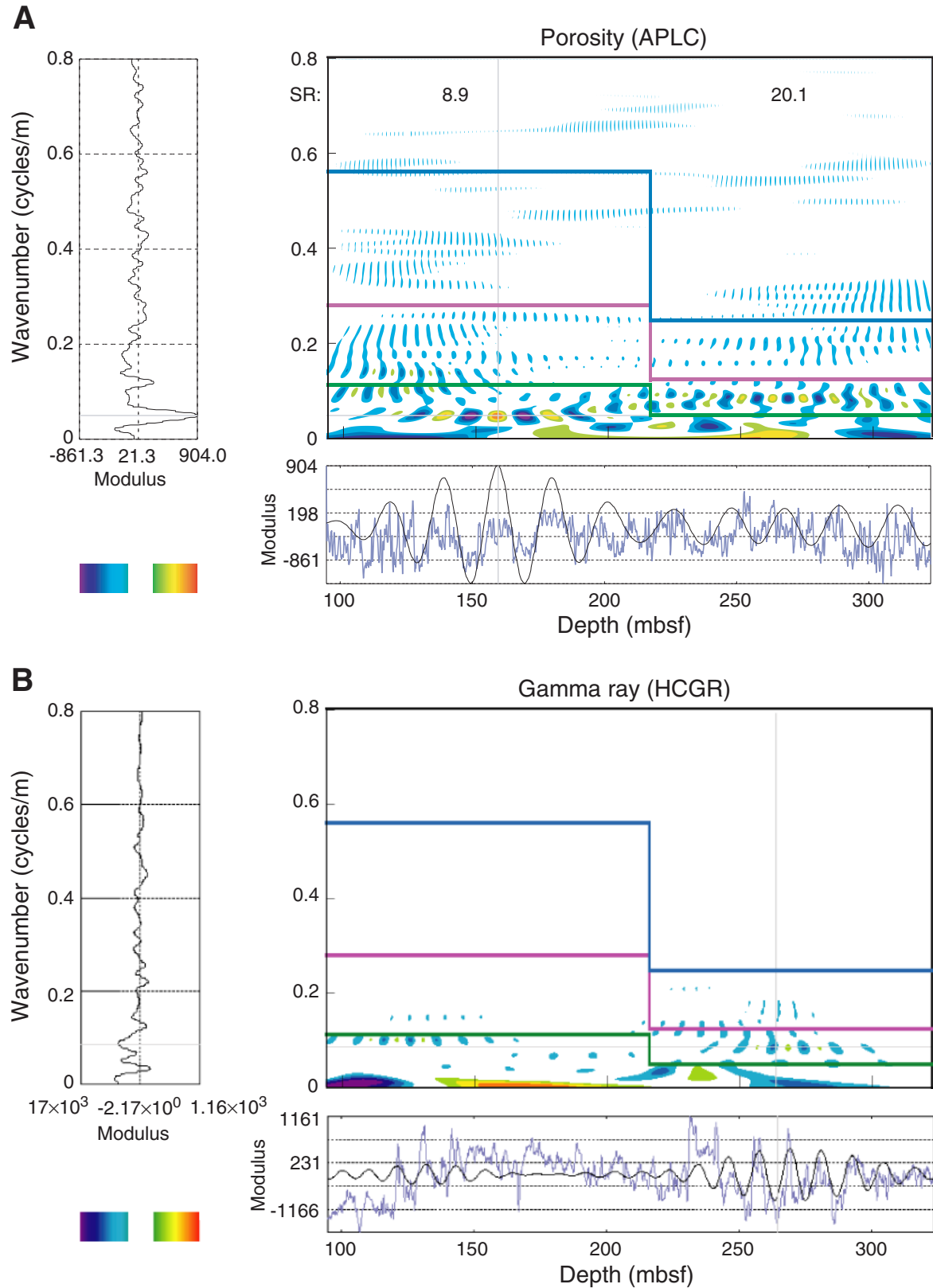


Figure F13 (continued). (C) Uranium log.

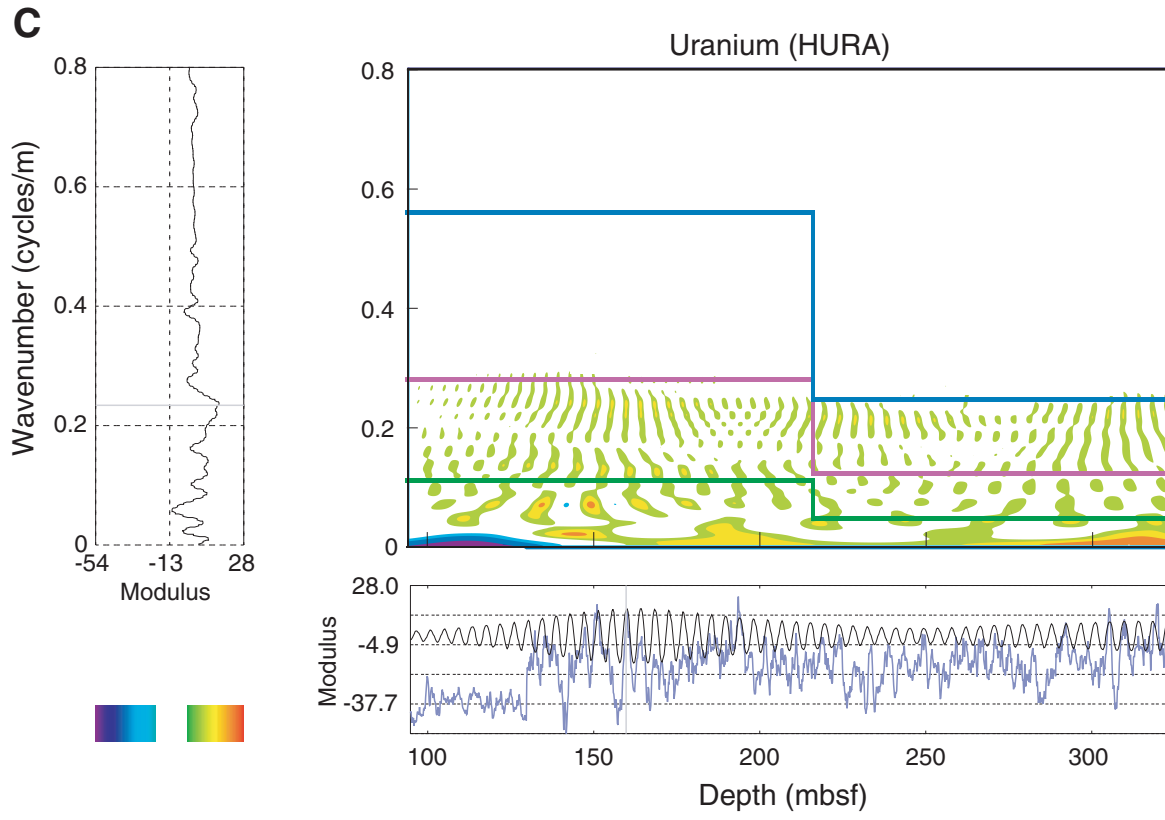


Figure F14. Hole 1096C, lower section (from 360 to 525 mbsf). Spectral maps for (A) the December insolation and (B) the truncated insolation signals. The presentation is the same as Figure F7, p. 24. SR = sedimentation rate.

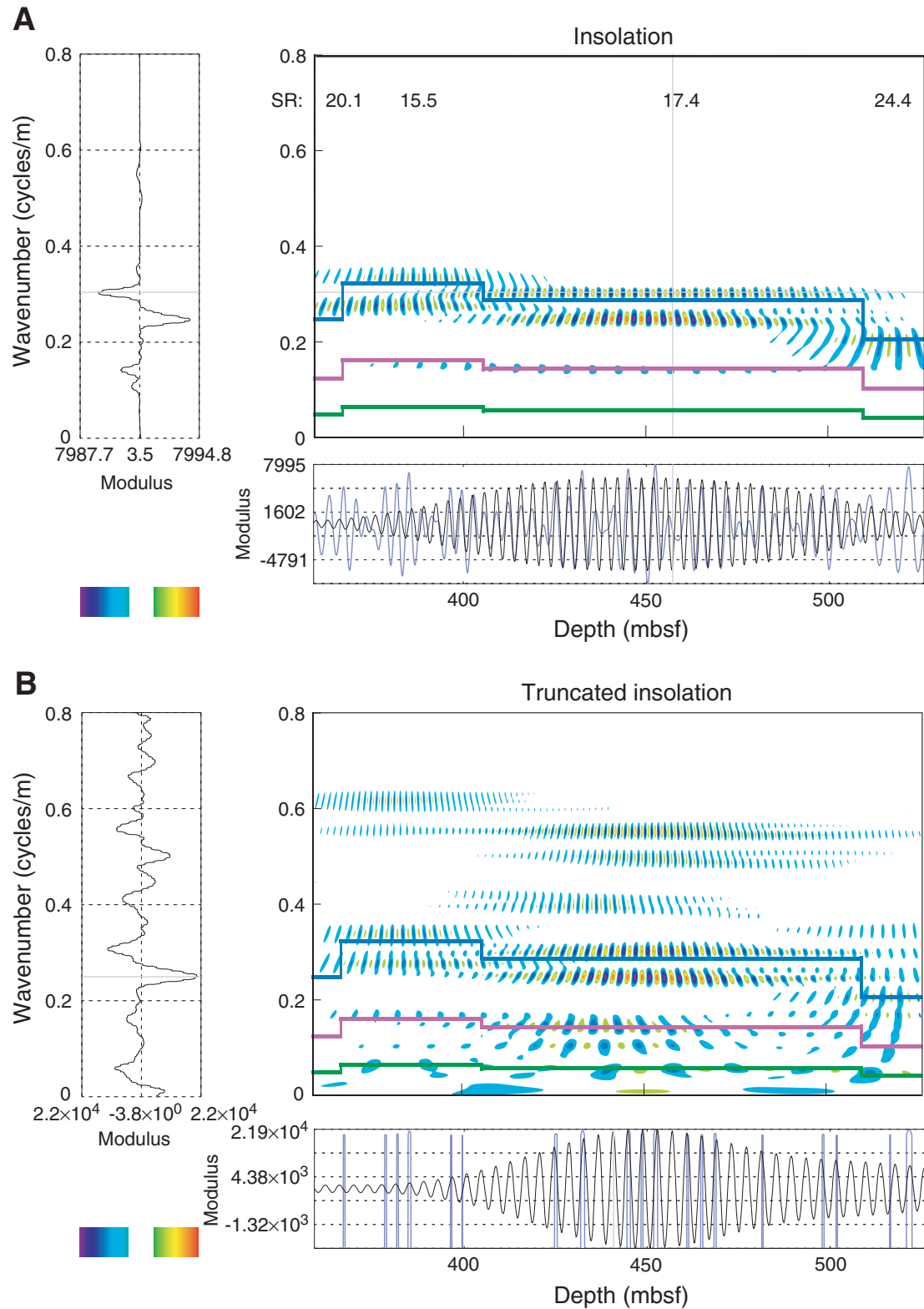
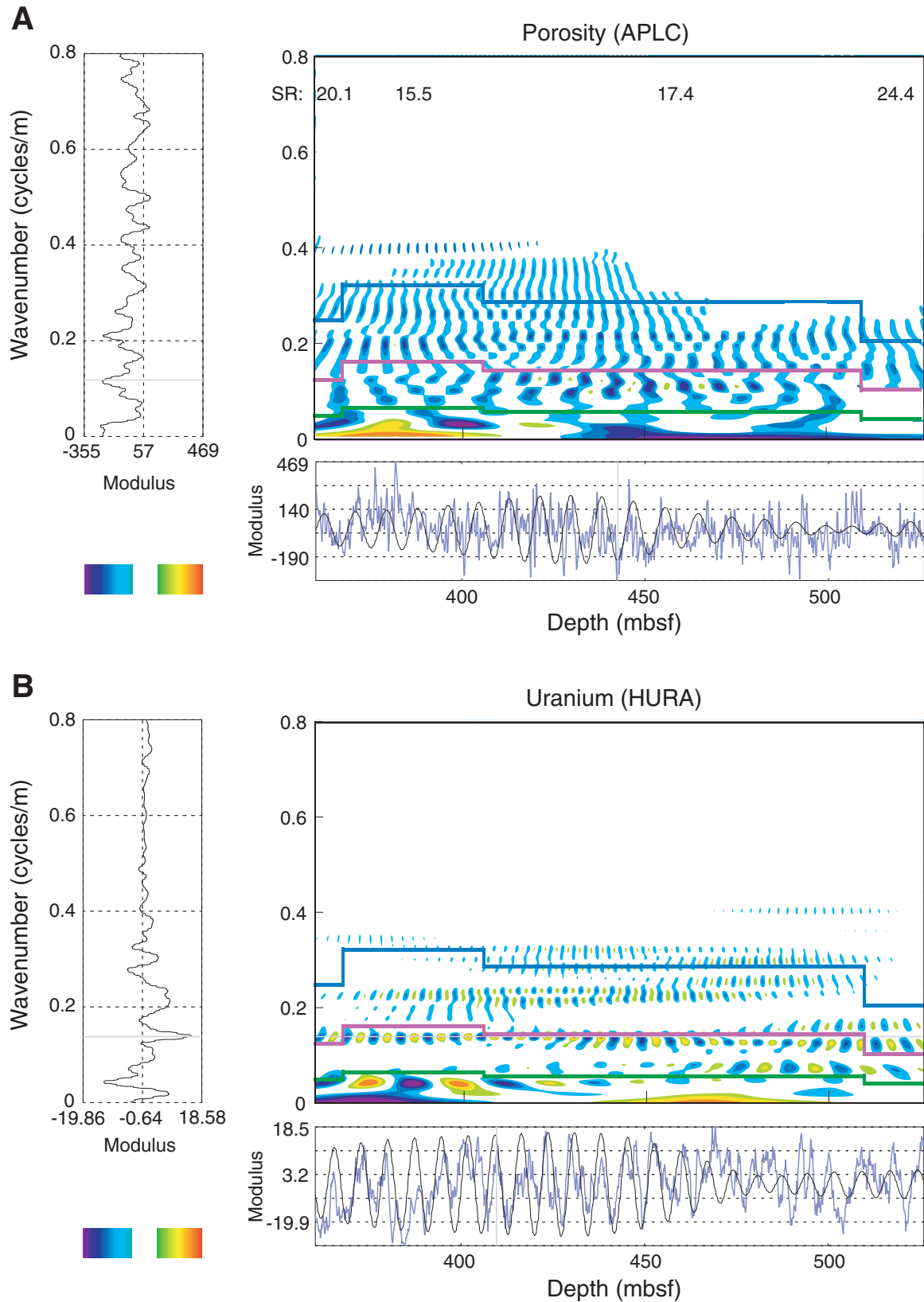


Figure F15. Hole 1096C, lower section (from 360 to 525 mbsf). Spectral maps for (A) porosity and (B) uranium logs. The presentation is the same as Figure F7, p. 24. SR = sedimentation rate.



**Table T1.** Results of wavelet analysis applied to the truncated insolation signal (modulated in depth using the geomagnetic reversals age model), the natural gamma ray, and the thorium/potassium ratio logs over the interval 165–545 mbsf, the bioturbated beds over the interval 100–435 mbsf, and the core magnetic susceptibility over the interval 320–436 mbsf, Hole 1095B.

| Wavenumber<br>(cycles/m)     | Period<br>(k.y.) | Depth<br>(mbsf) | Modulus      | Wavenumber<br>(cycles/m)       | Period<br>(k.y.) | Depth<br>(mbsf) | Modulus       |
|------------------------------|------------------|-----------------|--------------|--------------------------------|------------------|-----------------|---------------|
| Truncated insolation         |                  |                 |              | 0.250                          | 50               | 261–285         | 611           |
| 0.162                        | 121              | 165–220         | 2,650        | 0.595                          | 21               | 261–285         | 369           |
| 0.211                        | 94               | 165–220         | 2,926        | 0.070                          | 179              | 285–320         | 758           |
| 0.503                        | 40               | 165–220         | <b>5,084</b> | 0.121                          | 104              | 285–320         | 726           |
| 0.010                        | 1,430            | 220–254         | 3,774        | 0.198                          | 63               | 285–320         | 724           |
| 0.080                        | 84               | 220–254         | 3,404        | 0.220                          | 70               | 320–356         | 638           |
| 0.311                        | 23               | 220–254         | 5,084        | 0.394                          | 39               | 320–356         | 541           |
| 0.397                        | 18               | 220–254         | 4,184        | 0.440                          | 35               | 320–356         | 443           |
| 0.595                        | 12               | 220–254         | 4,075        | 0.496                          | 31               | 320–356         | 411           |
| 0.714                        | 10               | 220–254         | 3,800        | 0.641                          | 24               | 320–356         | 452           |
| 0.030                        | 392              | 254–308         | 2,950        | 0.060                          | 56               | 356–417         | 793           |
| 0.568                        | 20               | 254–308         | 4,194        | 0.101                          | 33               | 356–417         | 714           |
| 0.031                        | 439              | 308–343         | 2,613        | 0.152                          | 22               | 356–417         | 711           |
| 0.122                        | 128              | 308–343         | 2,918        | Th/K (log)                     |                  |                 |               |
| 0.149                        | 103              | 308–343         | 2,949        | 0.085                          | 245              | 165–215         | <b>36</b>     |
| 0.466                        | 34               | 308–343         | 2,850        | 0.138                          | 151              | 165–215         | 30            |
| 0.161                        | 27               | 343–389         | 3,129        | 0.202                          | 103              | 165–215         | 19            |
| 0.702                        | 22               | 343–389         | 3,722        | 0.254                          | 82               | 165–215         | 18            |
| 0.741                        | 21               | 343–389         | 3,211        | 0.070                          | 102              | 215–254         | 26            |
| 0.020                        | 133              | 389–428         | 2,622        | 0.171                          | 42               | 215–254         | 17            |
| 0.079                        | 42               | 389–428         | 3,961        | 0.090                          | 139              | 254–295         | 24            |
| 0.256                        | 129              | 389–428         | 3,100        | 0.131                          | 96               | 254–295         | 27            |
| 0.303                        | 11               | 389–428         | 3,313        | 0.169                          | 74               | 254–295         | 23            |
| 0.333                        | 10               | 389–428         | 3,200        | 0.403                          | 31               | 254–295         | 12            |
| 0.002                        | 600              | 456–491         | 3,350        | 0.211                          | 73               | 295–329         | 18            |
| 0.129                        | 59               | 491–520         | 2,371        | 0.270                          | 57               | 295–329         | 20            |
| 0.201                        | 39               | 491–520         | 2,815        | 0.040                          | 333              | 329–386         | 26            |
| 0.332                        | 23               | 491–520         | 2,852        | 0.111                          | 121              | 329–386         | 27            |
| 0.545                        | 14               | 491–520         | 2,487        | 0.139                          | 95               | 329–386         | 28            |
| 0.636                        | 12               | 491–520         | 1,992        | 0.111                          | 69               | 488–545         | 24            |
| Gamma ray (log)              |                  |                 |              | 0.150                          | 51               | 488–545         | 16            |
| 0.090                        | 218              | 162–208         | 162          | Magnetic susceptibility (core) |                  |                 |               |
| 0.129                        | 152              | 162–208         | 176          | 0.220                          | 70               | 317–352         | 4,085         |
| 0.202                        | 97               | 162–208         | 84           | 0.394                          | 39               | 317–352         | 3,523         |
| 0.104                        | 120              | 250–309         | 214          | 0.466                          | 33               | 317–352         | 1,648         |
| 0.132                        | 95               | 250–309         | 144          | 0.531                          | 29               | 317–352         | 2,280         |
| 0.238                        | 53               | 250–309         | 109          | 0.641                          | 24               | 317–352         | 1,730         |
| 0.297                        | 44               | 250–309         | 120          | 0.669                          | 23               | 317–352         | 1,880         |
| 0.032                        | 446              | 309–393         | 278          | 0.855                          | 18               | 317–352         | 2,705         |
| 0.029                        | 115              | 393–434         | <b>278</b>   | 1.026                          | 15               | 317–352         | 1,520         |
| 0.221                        | 15               | 393–434         | 128          | 1.282                          | 12               | 317–352         | 1,205         |
| 0.093                        | 82               | 470–545         | 208          | 1.399                          | 11               | 317–352         | 745           |
| 0.121                        | 63               | 470–545         | 149          | 0.110                          | 121              | 344–386         | 3,356         |
| 0.187                        | 41               | 470–545         | 128          | 0.310                          | 43               | 344–386         | 2,000         |
| Bioturbated intervals (core) |                  |                 |              | 0.342                          | 39               | 344–386         | 2,081         |
| 0.151                        | 370              | 57–98           | 630          | 0.952                          | 14               | 344–386         | 870           |
| 0.208                        | 265              | 57–98           | 554          | 0.190                          | 73               | 444–465         | <b>12,610</b> |
| 0.319                        | 174              | 57–98           | 552          | 0.302                          | 46               | 444–465         | 11,546        |
| 0.103                        | 200              | 98–156          | <b>971</b>   | 0.434                          | 34               | 444–465         | 7,034         |
| 0.228                        | 87               | 98–156          | 505          | 0.817                          | 17               | 444–465         | 10,007        |
| 0.357                        | 56               | 98–156          | 634          | 1.263                          | 11               | 444–465         | 10,911        |
| 0.100                        | 200              | 156–205         | 835          |                                |                  |                 |               |
| 0.230                        | 87               | 156–205         | 723          |                                |                  |                 |               |
| 0.317                        | 63               | 229–261         | 408          |                                |                  |                 |               |
| 0.400                        | 50               | 229–261         | 343          |                                |                  |                 |               |
| 0.465                        | 43               | 229–261         | 436          |                                |                  |                 |               |
| 0.169                        | 74               | 261–285         | 550          |                                |                  |                 |               |

Notes: The major wavenumbers are listed, with their corresponding period, computed using the appropriate sedimentation rate, depth of appearance, and maximum of modulus amplitude. The highest modulus is in bold.

**Table T2.** Detailed results of the wavelet analysis applied to core magnetic measurement over the subunit 320–390 mbsf, Hole 1095B.

| Depth (mbsf) | Wavenumber (cycles/m) | Magnetic reversals model |               | Radiolarian model |               | Diatom model |               |
|--------------|-----------------------|--------------------------|---------------|-------------------|---------------|--------------|---------------|
|              |                       | SR (cm/k.y.)             | Period (k.y.) | SR (cm/k.y.)      | Period (k.y.) | SR (cm/k.y.) | Period (k.y.) |
| 320–355      | 1.399                 | 6.5                      | 11            | 4.5               | 16            | 2.6          | 27            |
|              | 1.282                 | 6.5                      | 12            | 4.5               | 18            | 2.6          | 31            |
|              | 1.026                 | 6.5                      | 15            | 4.5               | 22            | 2.6          | 37            |
|              | 0.855                 | 6.5                      | 18            | 4.5               | 26            | 2.6          | 45            |
|              | 0.641                 | 6.5                      | 23            | 4.5               | 33            | 2.6          | 57            |
|              | 0.641                 | 6.5                      | 24            | 4.5               | 35            | 2.6          | 61            |
|              | 0.531                 | 6.5                      | 29            | 4.5               | 42            | 2.6          | 73            |
|              | 0.466                 | 6.5                      | 33            | 4.5               | 48            | 2.6          | 83            |
|              | 0.394                 | 6.5                      | 39            | 4.5               | 57            | 2.6          | 99            |
|              | 0.220                 | 6.5                      | 70            | 4.5               | 101           | 2.6          | 175           |
| 355–390      | 0.952                 | 7.5                      | 16            | 10.3              | 12            | 7.2          | 17            |
|              | 0.342                 | 7.5                      | 39            | 10.3              | 29            | 7.2          | 41            |
|              | 0.310                 | 7.5                      | 43            | 10.3              | 31            | 7.2          | 45            |
|              | 0.110                 | 7.5                      | 121           | 10.3              | 88            | 7.21         | 26            |

Notes: The major wavenumbers are listed, with their corresponding period, computed using the appropriate sedimentation rate for the three different age models. SR = sedimentation rate.

**Table T3.** Results of the wavelet analysis applied to the truncated insolation signal and the porosity, gamma ray, and uranium logs over the first interval (95–325 mbsf) and the reflectance over the interval 255–355 mbsf, Hole 1096C.

| Wavenumber<br>(cycles/m)    | Period<br>(k.y.) | Depth<br>(mbsf) | Modulus       |
|-----------------------------|------------------|-----------------|---------------|
| <b>Truncated insolation</b> |                  |                 |               |
| 0.028                       | 401              | 95–216          | 10,414        |
| 0.088                       | 112              | 95–216          | 7,880         |
| 0.118                       | 95               | 95–216          | 8,500         |
| 0.202                       | 55               | 95–216          | 7,323         |
| 0.272                       | 41               | 95–216          | 10,000        |
| 0.474                       | 24               | 95–216          | 12,058        |
| 0.500                       | 22               | 95–216          | 10,400        |
| 0.590                       | 19               | 95–216          | 12,260        |
| 0.616                       | 18               | 95–216          | 4,890         |
| 0.090                       | 55               | 170–270         | 7,655         |
| 0.218                       | 23               | 170–270         | 10,446        |
| 0.242                       | 21               | 180–270         | 8,173         |
| 0.330                       | 15               | 190–270         | 9,970         |
| 0.400                       | 12               | 190–270         | 4,375         |
| 0.052                       | 96               | 270–325         | 11,700        |
| 0.126                       | 42               | 200–325         | 10,300        |
| 0.210                       | 24               | 270–325         | 13,040        |
| 0.218                       | 23               | 270–325         | <b>15,480</b> |
| 0.264                       | 19               | 270–325         | 12,806        |
| 0.434                       | 11               | 270–325         | 10,170        |
| 0.482                       | 10               | 270–325         | 10,170        |
| 0.698                       | 7                | 270–325         | 6,800         |
| <b>Porosity (log)</b>       |                  |                 |               |
| 0.050                       | 225              | 95–216          | <b>902</b>    |
| 0.106                       | 106              | 95–170          | 480           |
| 0.142                       | 79               | 95–175          | 422           |
| 0.028                       | 178              | 175–270         | 610           |
| 0.072                       | 69               | 170–270         | 414           |
| 0.096                       | 52               | 170–270         | 410           |
| 0.062                       | 80               | 270–325         | 150           |
| 0.086                       | 58               | 220–325         | 645           |
| 0.104                       | 48               | 270–325         | 391           |

| Wavenumber<br>(cycles/m)  | Period<br>(k.y.) | Depth<br>(mbsf) | Modulus    |
|---------------------------|------------------|-----------------|------------|
| <b>Gamma ray (log)</b>    |                  |                 |            |
| 0.104                     | 108              | 95–175          | <b>510</b> |
| 0.068                     | 165              | 150–230         | 306        |
| 0.212                     | 23               | 170–270         | 208        |
| 0.052                     | 96               | 250–325         | 241        |
| 0.088                     | 56               | 216–325         | 505        |
| 0.116/0.138               | 36/43            | 200–300         | 300        |
| <b>Uranium (log)</b>      |                  |                 |            |
| 0.068                     | 165              | 95–185          | <b>17</b>  |
| 0.122                     | 92               | 95–185          | 10         |
| 0.238                     | 47               | 95–216          | 12         |
| 0.214                     | 23               | 210–275         | 7          |
| 0.022                     | 226              | 230–325         | 5          |
| 0.040                     | 124              | 190–325         | 12         |
| 0.100                     | 50               | 250–325         | 9          |
| 0.212                     | 23               | 275–325         | 6          |
| <b>Reflectance (core)</b> |                  |                 |            |
| 0.05/0.06                 | 83/100           | 270–350         | <b>271</b> |
| 0.104                     | 48               | 255–355         | 261        |
| 0.130                     | 38               | 255–355         | 170        |
| 0.192                     | 26               | 255–350         | 140        |
| 0.246                     | 20               | 270–350         | 131        |
| 0.276                     | 18               | 270–355         | 173        |
| 0.396                     | 13               | 270–355         | 112        |
| 0.452/0.466               | 11               | 270–355         | 141        |
| 0.698/0.726               | 7                | 300–355         | 132        |

Notes: The major wavenumbers are listed, with their corresponding period, computed using the appropriate sedimentation rate, depth of appearance, and maximum of modulus amplitude. The highest modulus is in bold.

**Table T4.** Results of the wavelet analysis applied to the truncated insolation signal and the porosity and uranium logs over the second interval (360–525 mbsf), Hole 1096C.

| Wavenumber<br>(cycles/m) | Period<br>(k.y.) | Depth<br>(mbsf) | Modulus       |
|--------------------------|------------------|-----------------|---------------|
| Truncated insolation     |                  |                 |               |
| 0.058                    | 99 or 111        | 360–435         | 11,706        |
| 0.172                    | 33 or 37         | 360–450         | 7,029         |
| 0.278                    | 21 or 23         | 360–450         | 11,645        |
| 0.342                    | 17 or 19         | 360–435         | 10,130        |
| 0.612/0.624              | 9 or 10          | 360–435         | 10,195        |
| 0.106                    | 54               | 420–480         | 11,031        |
| 0.146                    | 39               | 390–480         | 13,270        |
| 0.250                    | 23               | 390–480         | 17,563        |
| 0.304                    | 19               | 390–480         | <b>21,926</b> |
| 0.396/0.414              | 14               | 400–480         | 9,827         |
| 0.498/0.504              | 11               | 400–485         | 10,260        |
| 0.550/0.558              | 10               | 390–490         | 16,599        |
| 0.056                    | 103              | 420–525         | 11,071        |
| 0.174                    | 33               | 455–525         | 9,371         |
| 0.250                    | 23               | 480–525         | 13,345        |
| 0.304/0.310              | 19               | 400–525         | 17,180        |
| 0.350                    | 16               | 460–525         | 7,134         |
| Porosity (log)           |                  |                 |               |
| 0.028                    | 205 or 230       | 360–450         | <b>340</b>    |
| 0.052                    | 110 or 124       | 360–450         | 150           |
| 0.078                    | 74 or 83         | 360–430         | 155           |
| 0.092                    | 62 or 70         | 360–475         | 237           |
| 0.120                    | 48 or 54         | 360–480         | 230           |
| 0.196                    | 29 or 33         | 360–430         | 220           |
| 0.260                    | 22 or 25         | 360–480         | 185           |
| 0.394                    | 15 or 16         | 360–440         | 174           |
| 0.150/0.164              | 35/38            | 425–490         | 164           |
| 0.052                    | 79 or 110        | 480–525         | 150           |
| 0.078                    | 74               | 450–525         | 155           |
| 0.104                    | 55               | 430–525         | 257           |
| 0.146                    | 39               | 430–525         | 162           |
| 0.200                    | 20 or 29         | 470–525         | 140           |
| 0.212                    | 19 or 27         | 390–525         | 220           |
| Uranium (log)            |                  |                 |               |
| 0.040                    | 144 or 161       | 360–450         | <b>20</b>     |
| 0.072                    | 80 or 90         | 360–450         | 7             |
| 0.140                    | 41 or 46         | 360–480         | 16            |
| 0.180                    | 32 or 36         | 360–450         | 6             |
| 0.196                    | 29 or 33         | 360–450         | 6             |
| 0.214                    | 27 or 30         | 390–480         | 9             |
| 0.226                    | 25 or 29         | 360–420         | 8             |
| 0.234                    | 25 or 28         | 360–460         | 9             |
| 0.320                    | 18 or 20         | 370–520         | 7             |
| 0.074                    | 78               | 450–525         | 11            |
| 0.122                    | 61               | 450–525         | 12            |
| 0.162                    | 35               | 460–525         | 8             |
| 0.226                    | 25               | 440–500         | 8             |
| 0.282                    | 20               | 400–510         | 8             |
| 0.294                    | 19               | 450–525         | 8             |

Notes: The major wavenumbers are listed, with their corresponding period, computed using the appropriate sedimentation rate, depth of appearance, and maximum of modulus amplitude. The highest modulus is in bold.

**Table T5.** Results of wavelet analysis applied to thorium/potassium ratio logs for the interval 165–195 mbsf, Hole 1095B.

| Wavenumber<br>(cycles/m) | Period (k.y.)                       |                          |                     |
|--------------------------|-------------------------------------|--------------------------|---------------------|
|                          | Geomagnetic<br>reversal<br>SR = 4.8 | Radiolarian<br>SR = 17.1 | Diatom<br>SR = 18.7 |
| 0.254                    | 82                                  | 23                       | 21                  |
| 0.202                    | 103                                 | 28                       | 26                  |
| 0.138                    | 151                                 | 42                       | 39                  |
| 0.085                    | 245                                 | 68                       | 63                  |

Notes: The periods are computed using age models based on the geomagnetic reversals and radiolarian and diatom data. The major wavenumbers are listed, with their corresponding period, computed using the appropriate sedimentation rate. SR = sedimentation rate (in centimeters per thousand years).

**CHAPTER NOTE\***

- N1. Weber, M.E., submitted. Late Neogene (0–8 Ma) orbital forcing in the eastern equatorial Pacific: implications to the emerge of the isthmus of panama and the initiation of the Northern Hemisphere glaciation. *Palaeogeogr., Palaeoclimatol., Palaeoecol.*